STATE OF OREGON
DEPARTMENT OF GEOLOGY AND MINERAL INDUSTRIES
VICKI S. McCONNELL, STATE GEOLOGIST

Geologic Map of the Hawks Valley - Lone Mountain Region, Harney County, Oregon

2011

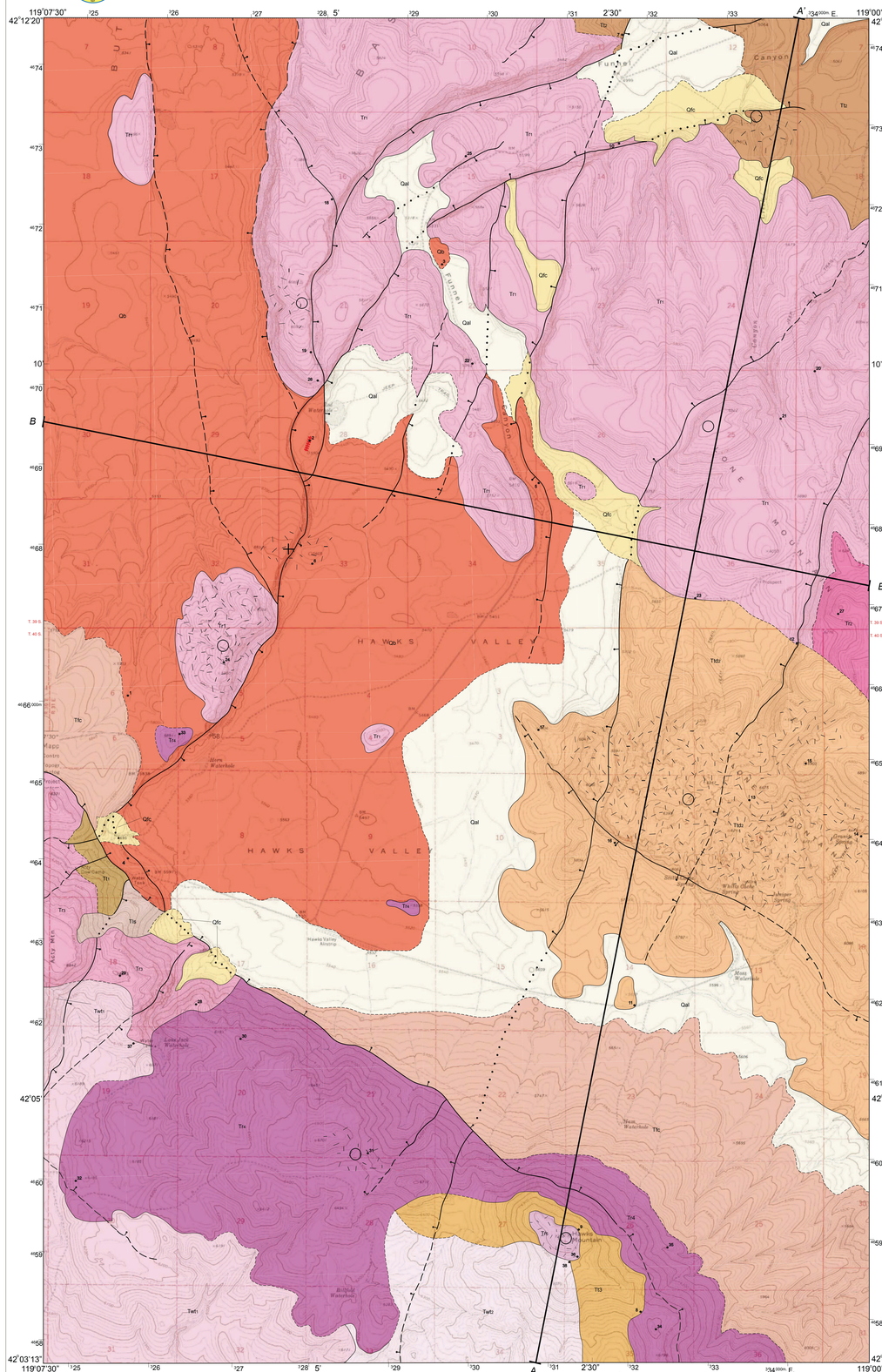

State of Oregon
Oregon Department of Geology and Mineral Industries
Vicki S. McConnell, State Geologist

OPEN-FILE REPORT O-11-12

GEOLOGIC MAP OF THE HAWKS VALLEY-LONE MOUNTAIN REGION, HARNEY COUNTY, OREGON.

By: Alicja Wypych[1], William K. Hart[1], Kaleb C. Scarberry[2], Kelly C. McHugh[1], Stephen A. Pasquale[1] and Paul W. Legge[1]

2011

[1] Geology, Miami University, 114 Shideler Hall, Oxford, OH 45056

[2] Geosciences, Colorado State University, 1482 Campus Delivery, Fort Collins, CO 80523-1482

NOTICE

The views and conclusions contained in this document are those of the authors and should not be interpreted as necessarily representing the official policies, either expressed or implied, of the U.S. government. The results and conclusions of this report are necessarily based on limited geologic and geophysical data. At any given site in any map area, site-specific data could give results that differ from those shown in this report. **This report cannot replace site-specific investigations.** The hazards of an individual site should be assessed through geotechnical or engineering geology investigation by qualified practitioners.

Oregon Department of Geology and Mineral Industries Open-File Report O-11-12
Published in conformance with ORS 516.030

For copies of this publication or other information about Oregon's geology and natural resources, contact:

Nature of the Northwest Information Center
800 NE Oregon Street #28, Suite 965
Portland, Oregon 97232
(971) 673-2331
http://www.naturenw.org

For additional information:
Administrative Offices
800 NE Oregon Street #28, Suite 965
Portland, OR 97232
Telephone (971) 673-1555 Fax (971) 673-1562
http://www.oregongeology.org
http://egov.oregon.gov/DOGAMI/

CONTENTS

PLATE 1

1:24,000-scale geologic map and cross sections of the Hawks Valley-Lone Mountain Region, Harney County, Oregon

LIST OF FIGURES

LIST OF TABLES

ABSTRACT

New geologic mapping and supporting analytical work combined with previous observations and data reveal a complex interplay between regional mafic magmatism, regional fault patterns, and local silicic magma generation and evolution in the Hawks Valley-Lone Mountain area of southeastern Oregon. This portion of Oregon provides an ideal natural laboratory for field-based studies of mid-Miocene and younger extensional tectonism and magmatism due to well-developed fault patterns and near continuous volcanism since ~16.6 Ma. Our observations and data indicate that the Hawks Valley-Lone Mountain (HVLM) area is characterized by a NW-striking structural valley that cuts an ~150 km^2 mid-Miocene, trachyte-trachydacite-rhyolite volcanic complex. New radiometric ages and stratigraphic relationships indicate that the bulk of HVLM volcanism occurred during a <1 m.y. window synchronous with or shortly following eruption of the Steens Basalt from fissures in the Steens-Pueblo Mountains located less than 20 km to the east.

Numerous 16.3±0.3 Ma silicic units, most emanating from at least eight local vents, are distinguished based on field relationships, petrography, and major/trace element geochemistry. Resorbed alkali feldspar and resorbed and complexly-zoned plagioclase indicate that magma mixing and/or crustal assimilation were important petrogenetic processes. Geochemical parameters support these observations and require a major role for crystal fractionation in the evolution of the HVLM silicic materials. The HVLM's structural complexities and its proximity to exposures of temporally equivalent Steens flood basalt eruptive loci suggest that basaltic input into the crust stimulated local melt production, the establishment of multiple small upper-level magmatic systems along regional lithospheric weaknesses, and open system differentiation leading to the silicic suite. After a more than 15 m.y. hiatus local HVLM volcanism resumed with the eruption of 0.8-0.5 Ma low-K, high-Al olivine tholeiite (HAOT) lavas characteristic of the High Lava Plains region and of relatively shallow basalt melt generation processes.

The Quaternary HVLM magmatism produced small volumes of basalt that were erupted along and offset by reactivated NNE-striking structures. In contrast, NW-striking faults, with rare exception, displace only the mid-Miocene silicic lavas and are in turn cut by NNE-striking structures. Additionally, there is a strong association of silicic vent locations and these structural trends. Numerous 16.3-16.5 Ma rhyolite/trachyte vents are situated at or near the intersection of younger NNE- and NW-striking structures indicating that both structural trends were active and available for magma passage in the mid-Miocene.

INTRODUCTION

This report details aspects of the geologic history of the Hawks Valley-Lone Mountain area (HVLM) of southeastern Oregon and comments on the interrelationships between faulting and magmatism in this region. We present the results of new geologic mapping and supporting analytical work combined with previous observations and data for a ~175 km^2 area located west of the Steens-Pueblo Mountains in southeastern Oregon (Figure 1). The centerpiece of these efforts is the 1:24,000 scale "Geologic Map of the Hawks Valley-Lone Mountain Region, Harney County, Oregon" (Plate 1). The principal goal of the mapping project was to further document the relationship between mid-Miocene silicic volcanism, extensional deformation, and the impact of the Yellowstone hotspot on the lithosphere; the first-order manifestation of this is taken to be represented by the spatial and temporal character of regional flood basalt volcanism (Steens and Columbia River basalts).

The HVLM exemplifies regional relationships between extensional tectonics and magmatism. Volcanism and faulting since ~16.6 Ma has created a region optimal for field-based studies aimed at investigating factors controlling the formation and modification of continental lithosphere. The HVLM lies ~50 km north of the Nevada-Oregon border in a transitional location between the High Lava Plains and northwest Basin and Range provinces (Carlson and Hart, 1987; Colgan et al., 2006; Lerch et al., 2008)(Figure 1). Additionally, the HVLM is in the western portion of the Idaho-Oregon-Nevada (ION) region that serves as the intersection of three mid-Miocene to Recent tectonomagmatic features; the NE-striking Snake River Plain-Yellowstone trend (SRP), the NW-striking High Lava Plains-Newberry trend (HLP), and the NNW-

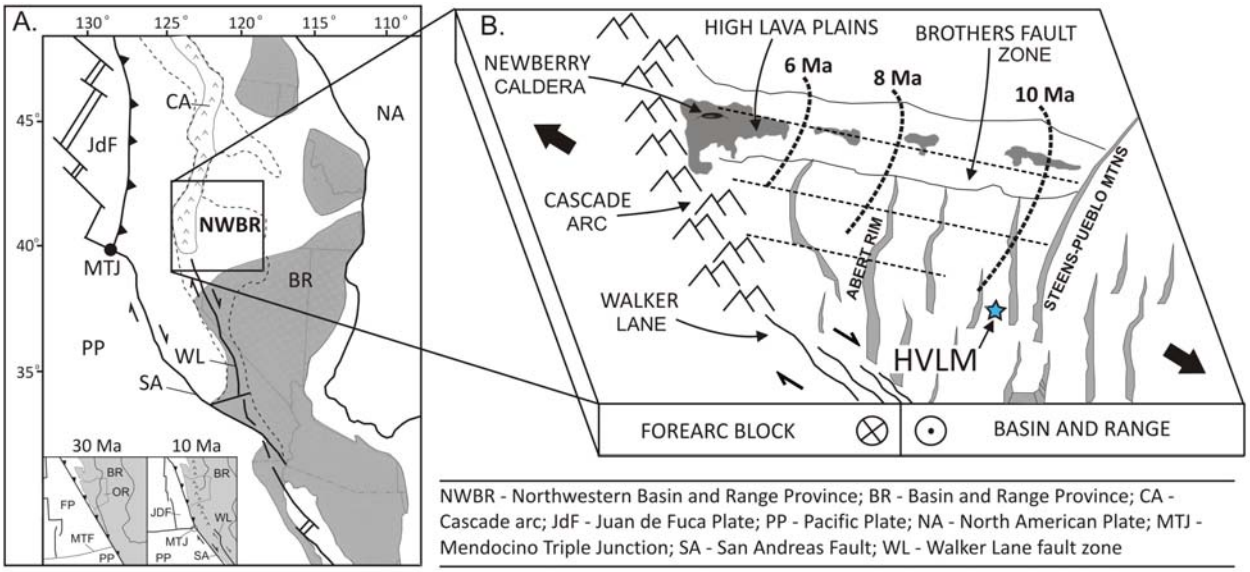

Figure 1: (A) Tectonic setting and stages (inset) in the Late Cenozoic development of the transform margin and Basin and Range of western North America (after Atwater and Stock, 1998; Faulds et al., 2005). Areas of major (50-100%) and minor (<10-20%) Cenozoic extension are shown by dark and dotted patterns, respectively (after Stewart, 1998). The northwestern Basin and Range Province (NWBR) is a broad zone of active seismicity (after Pezzopane and Weldon, 1993) and minor extension located at the tip of the Walker Lane fault zone. (B) Fault kinematics of the NWBR with regional extension direction shown by large arrows. Dextral shear from the Walker Lane is transferred into a system of extensional faults that diminish along-strike to the north into the High Lava Plains. Isochrons that in general bracket the age of silicic centers (after Jordan et al., 2004) shown as thick dashed lines. Concentrated bands of NW-striking normal faults (thin dashed lines) form transverse to the grain of Basin and Range faults (light shaded polygons). The Brothers Fault zone, the northernmost of these zones, is defined by a track of Quaternary basalts (dark shaded polygons). The Hawks Valley-Lone Mountain area (HVLM) is depicted by the blue star.

striking Northern Nevada Rift (Pierce and Morgan, 1992; Zoback et al., 1994; John et al., 2000; Jordan et al., 2004; Brueseke et al., 2008; Meigs et al., 2009)(Figure 2). Mid-Miocene to Recent basaltic and bimodal basalt-rhyolite volcanism and extension in the northwestern United States is associated with processes related to convergence between the North American Plate and various oceanic plates and terranes coupled with the effects of the Yellowstone hotspot (e.g., Christiansen and Lipman, 1972; Carlson and Hart, 1987; Pierce and Morgan, 1992; Camp and Ross, 2004; Jordan et al., 2004; Pierce and Morgan, 2009). The exact causes and effects of the Yellowstone hotspot are not yet fully understood.

Following a brief magmatic hiatus (ca. 19-17 Ma) that marked a period of significant regional tectonic change, major outpourings of basaltic magma (Steens and Columbia River basalts) initiated from vent locations extending for over 1000 km from SE Washington to central Nevada, and from isolated locations to the east and west (e.g., Carlson and Hart, 1987; Zoback et al., 1994; Camp and Ross, 2004; Brueseke et al., 2007). The development of compositionally diverse, although fundamentally bimodal volcanic fields and silicic dome (HVLM) and caldera complexes in the ION region was synchronous with or followed shortly after flood basalt activity (Brueseke et al., 2008 and references therein). ION area mid-Miocene silicic volcanism became distributed into opposing time-transgressive tracks (SRP and HLP) during the Late Miocene (Figure 2). In both cases the spatial-temporal progression is marked by initiation of silicic eruptive centers, with basaltic volcanism following and remaining locally active to the present-day. The HLP, a locus of basalt-rhyolite volcanism after 10 Ma, generally coincides with the Brothers Fault Zone (e.g., Meigs et al., 2009 and references therein), which is a broad NW-striking zone of small en-echelon faults (Lawrence, 1976) (Figures 1 and 2).

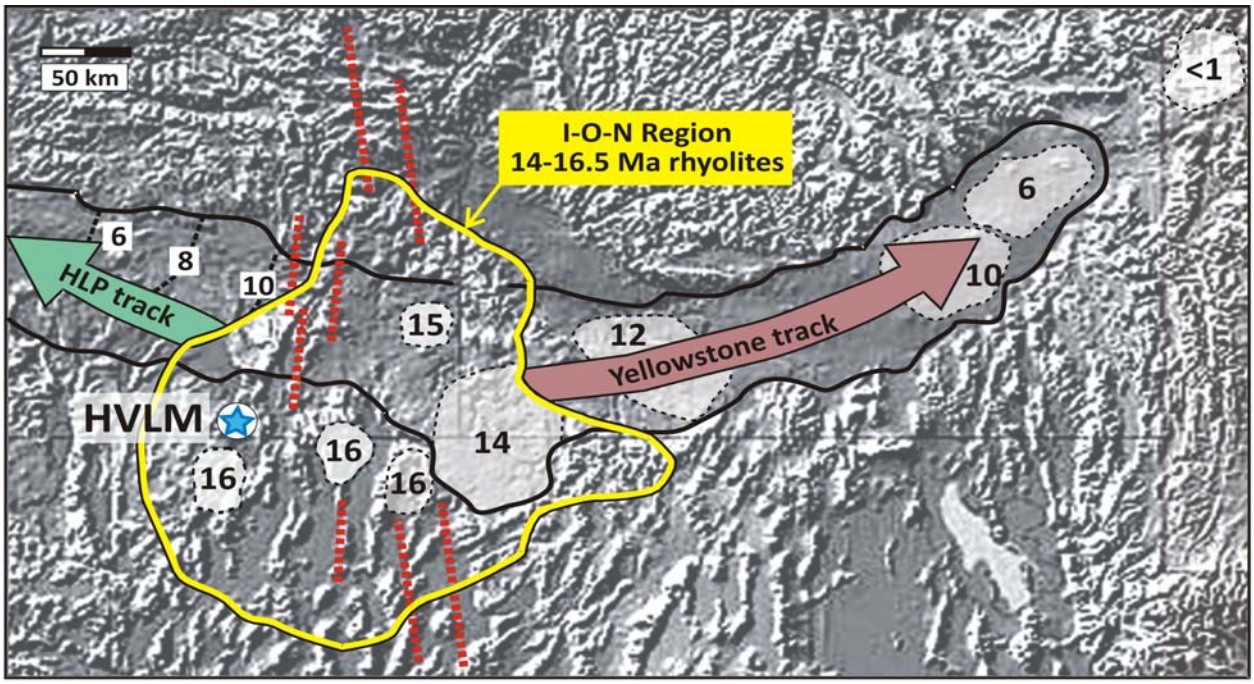

Figure 2: Shaded-relief map illustrating the distribution of mid Miocene rhyolite volcanism at the northern edge of the Basin and Range Province, Idaho-Oregon-Nevada (I-O-N) Region. Oppositely migrating tracks of rhyolite volcanism of Yellowstone and the High Lava Plains (HLP) are shown. Volcanic fields and calderas with representative ages in Ma after Pierce and Morgan (1992), Castor and Henry (2000), and Brueseke et al. (2008). Mid-Miocene dikes and rift features (red dashed lines) and extent of 14-16.5 Ma rhyolite are pictured. The age (in Ma) of rhyolite centers along the HLP track (dashed line) after Jordan et al. (2004). HVLM represented by blue star.

The northwest Basin and Range (NWBR) extends to the Cascade volcanic arc in the west and the HLP/Brothers Fault Zone in the north. Tectonic controls on the NWBR are influenced by Middle- to Late-Miocene development and northward propagation of the Walker Lane, a younger complement to the San Andreas transform system (e.g., Wesnousky, 2005)(Figure 1). The Walker Lane transform system is likely influencing the NWBR by causing extension or counterclockwise block rotation at its western boundary (Pezzopane and Weldon, 1993; Faulds et al., 2005; Scarberry et al., 2010). Deformation south of the HLP is accommodated along faults that exhibit two principal strike directions: NNE and NW, as observed in the HVLM (Pezzopane and Weldon, 1993; Crider, 2001; Scarberry et al., 2010)(Figures 2 and 3). NNE-striking, large offset (100's of meters) normal faults form the dominant topographic features of the landscape. Isolated zones of NW-striking, small offset (10's of meters) oblique-slip faults intersect and are overprinted by the NNE-striking Basin and Range fabric (e.g., Walker and MacLeod, 1991 and references therein). Structures within the NWBR formed after ~10 Ma and NW-striking faults may form in advance of NNE-striking Basin and Range faults in any particular location. Extension of the NWBR along NNE-striking Basin and Range style faults is believed to be minor compared with the central Basin and Range. For example a field-based structural study across Abert Rim located west of the HVLM map area (Figure 1) indicates that NW-striking faults formed prior to the principal NNE-striking escarpment and that net extension since 16 Ma is on the order of ~3% (Scarberry et al., 2010), consistent with other recent regional estimates of <17-20% (e.g., Lerch et al., 2008).

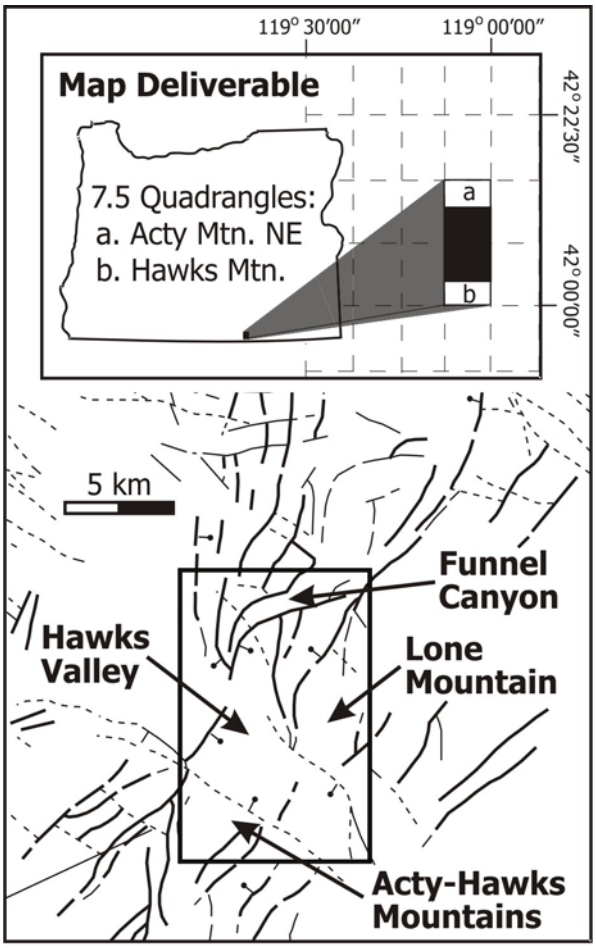

Figure 3: Index (top) and structure (bottom) maps of 1:24000 scale geologic mapping area encompassing the southern portion of the Acty Mountain NE Quadrangle and the northern portion of the Hawks Mountain Quadrangle. Dashed lines on index map define 7.5' quadrangles. Faults on structure map (after Walker and MacLeod, 1991) that trend NNE (solid) and NNW (dashed) are shown with ball on down dropped side.

PERSONNEL AND METHODOLOGY

New 1:24,000 scale geologic mapping was undertaken during summer 2009 by Alicja Wypych as a component of her Ph.D. research at Miami University. Miami postdoctoral fellow Dr. Kaleb Scarberry and undergraduate Geology students Kelly McHugh and Laura Flores joined Ms. Wypych for the 2009 field campaign. That field work was supported by the U.S. Geological Survey, National Cooperative Geologic Mapping Program, under assistance Award No. G09AC00145. Project Principle Investigator and award recipient Dr. William Hart spent time in the field with the 2009 team and returned with Ms. McHugh for additional mapping during summer 2010. Ms.

Wypych remains a Ph.D. candidate in Geology at Miami University and Dr. Scarberry now holds a teaching position at Colorado State University. Ms. McHugh is in her senior year at Miami and is working on a senior thesis involving the young HVLM basalts. Ms. Flores is presently on leave from her studies attending to family matters. Dr. Hart served as mentor and overseer of progress on this project at every stage, and is primary advisor for the research of Ms. Wypych and Ms. McHugh.

The 2009-10 field mapping was conducted using 1:24,000 scale topographic base maps and accompanying aerial photographs with the assistance of hand-held GPS receivers. This mapping built on and extended previous field and analytical efforts by Legge (1988) and Pasquale and Hart (2006). Samples of representative materials were collected during field campaigns in 1985, 2004, 2009, and 2010. The preliminary results of this work including earlier drafts of the geologic map were presented at the 2009 Annual Meeting and 2010 Cordilleran Meeting of the Geological Society of America (Wypych et al., 2009; McHugh et al., 2010).

Samples for whole-rock chemical, K-Ar, and Ar-Ar analysis (Tables 1-3) were collected to minimize secondary alteration and were processed to minimize laboratory contamination. All samples were either cut into slabs on a water-cooled diamond saw or split into pieces with a hydraulic splitter followed by removal of alteration and metallic residue via a water-cooled silicon carbide belt sander, after which they were washed in deionized water and dried at room temperature. Material was further processed for whole rock geochemical analysis by sequential size reduction to <0.15 mm via steel jaw crusher, alumina ceramic disc mill, and alumina ceramic shatterbox mill. Material further processed for geochronology was crushed in a steel mortar and pestle and/or steel jaw crusher to size fractions of ~0.5-1.7 mm (whole rock K-Ar) or ~0.25-0.5 mm (Ar-Ar), washed in deionized water and dried at 40°C for ~12 hours. For the Ar-Ar analyses, feldspars were isolated as a non-magnetic fraction at 2.0 amperes with a Frantz Magnetic Barrier Separator.

$^{40}Ar/^{39}Ar$ ages were obtained at Oregon State University (OSU)(Table 1). Samples were irradiated at the OSU TRIGA reactor for 7 hours at 1MW power, and the neutron flux was monitored using the FCT-3 biotite standard (28.03 Ma; Renne et al., 1994). Analyses were done with a Mass Analyzer Products MAP-215/50 operating in peak-hopping mode. Plateau ages were preferred for all samples. Details of the procedures used at Oregon State University are provided in Jordan et al. (2004). K-Ar ages (Table 2) were determined at Case Western Reserve University using a low volume extraction system coupled with a MS-10 mass spectrometer following the procedures outlined in Hart et al. (1984) and Hart and Carlson (1985). Decay constants used for Ar-Ar and K-Ar are those recommended by Steiger and Jäger (1977).

Major and trace element concentrations (Table 3) were determined by x-ray fluorescence spectrometry (XRF) at Franklin and Marshall College following the procedures outlined by Mertzman (2000) and/or by direct current argon plasma optical emission spectroscopy (DCP-OES) at Miami University following the procedures of Katoh et al. (1999) as described for whole rock samples in Brueseke and Hart (2008).

VOLCANIC STRATIGRAPHY

Figure 3 provides a detailed view of the HVLM study area in the context of dominant regional structural elements, and illustrates that the map area displayed in Plate 1 encompasses portions of the Acty Mountain NE and Hawks Mountain 7.5' Quadrangles. The volcanic stratigraphy of the HVLM map area is dominated by mid-Miocene trachyte-trachydacite-rhyolite lava flows, dikes/plugs, and proximal vent deposits (Legge, 1988; Pasquale and Hart, 2006; Wypych et al., 2009; McHugh et al., 2010; this study) that on a broader scale represent the silicic endmember of voluminous regional mid-Miocene and younger bimodal volcanism (e.g., Pierce and Morgan, 1992;

Castor and Henry, 2000; Brueseke et al., 2008). This regional silicic volcanism also is locally represented by distal ash-flow sheets interpreted as belonging to the Idaho Canyon Tuff/Oregon Canyon Tuff (Rytuba and McKee, 1984; Green, 1984; Walker and McLeod, 1991; Colgan et al., 2006; Henry et al., 2006; Lerch et al., 2008). HVLM area basaltic magmatism is represented by tholeiitic and mildly alkaline lava flows ranging in age from ~16.6 Ma to <1 Ma (e.g., Green, 1984; Hart et al., 1984; Carlson and Hart, 1987; Legge, 1988; Walker and McLeod, 1991), with only young tholeiitic eruptive products and vents (0.6±0.3 Ma) exposed in the project map area.

Thirteen volcanic stratigraphic units and numerous vents/vent regions are defined for the HVLM project area and are introduced below. In addition, the regionally important Steens Basalt, which is interpreted to underlie the HVLM, is included in the descriptions. The reader is referred to the accompanying 1:24,000 scale "Geologic Map of the Hawks Valley-Lone Mountain Region, Harney County, Oregon" (Plate 1) and to Figure 3 for additional details and for specific location references. Due to non-continuous exposures and a paucity of observed stratigraphic relationships between many of the units, the stratigraphic descriptions are grouped into spatial and/or temporal packages within which units are listed from oldest to youngest. Figure 4 provides a summary of the mid-Miocene stratigraphic interpretations and chronologic data for the HVLM map area.

Middle Miocene Flood Basalt

Steens Basalt: 16.6 ± 0.1 Ma

The Steens Basalt is widespread across southern Oregon and adjacent regions with eruptive localities concentrated in but not limited to the Steens-Pueblo Mountains, and thick stratigraphic sections prominently exposed to the west and east of the HVLM (e.g., Carlson and Hart, 1987; Brueseke et al., 2007). This basalt is not exposed in the HVLM, but multiple HVLM silicic units appear to on-lap Steens Basalt to the E-NE of the map area, and the Idaho Canyon Tuff/Oregon Canyon Tuff overlies Steens Basalt to the east and south of the map area. Using the same Ar calculation parameters employed in this study an age of 16.6 ± 0.1 is suggested for the Steens Basalt that is interpreted to underlie the HVLM (e.g., Henry et al., 2006; Jarboe et al., 2010 and references therein).

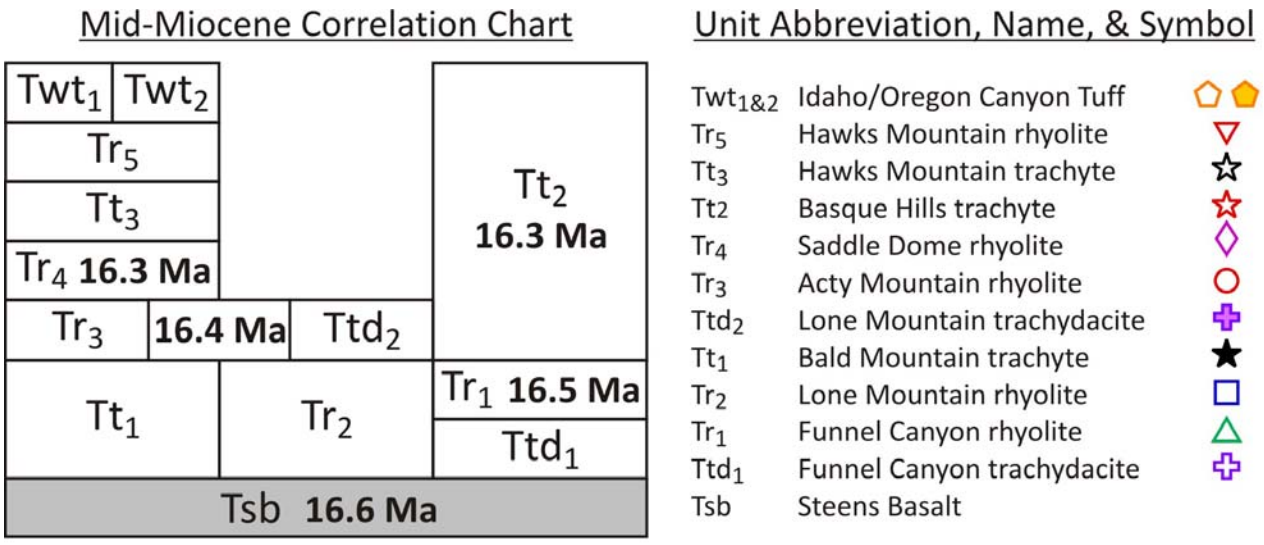

Figure 4: Middle Miocene stratigraphy, chronology, and map unit abbreviations and names. Also pictured are symbols associated with these units as they appear on the geochemical plots.

Table 1: ^{40}Ar / ^{39}Ar Radiometric Age Determinations

Sample	Map # / Unit	Material	Plateau (Ma)				Normal Isochron (Ma)		Total Fusion (Ma)
			Age ± 2 σ	Steps	$\%^{39}Ar$	MSWD	Age ± 2 σ	$^{40}Ar/^{36}Ar$ ± 2 σ	Age ± 2 σ
PL-100	13 / Ttd2	feldspar	**16.40 ± 0.19**	8/11	97.0	1.98	16.36 ± 0.19	376.7 ± 43.4	16.40 ± 0.19
PL-162	14 / Ttd2	feldspar	**16.46 ± 0.21**	10/12	98.8	1.67	16.43 ± 0.22	316.3 ± 53.0	16.45 ± 0.21
SP04-10	19 / Tr1	feldspar	**16.51 ± 0.25**	8/11	71.2	0.32	16.52 ± 0.25	294.8 ± 6.3	16.64 ± 0.25
SP04-25	nom / Tr3	feldspar	**16.39 ± 0.17**	14/14	100.0	1.76	16.38 ± 0.18	304.2 ± 17.5	16.39 ± 0.17
SP04-32	32 / Tr4	feldspar	**16.33 ± 0.17**	12/12	100.0	2.18	16.36 ± 0.17	286.7 ± 19.8	16.33 ± 0.17

Plateau age data includes number of steps in the plateau (steps in plateau / total steps) and % ^{39}Ar in plateau. Samples not within map area indicated as nom.

Table 2: K/Ar Radiometric Age Determinations

Sample	Map # / Unit	Material	Age ± 2 σ	Weight (gm)	K_2O (wt%)	$^{40}Ar^*$ (m/gm)	$^{40}Ar^*$ (%)
PL-193	1 / Qb	whole rock	**0.47 ± 0.23**	5.012	0.246	1.65×10^{-13}	0.83
PL-69	3 / Qb	whole rock	**0.81 ± 0.25**	5.035	0.242	2.83×10^{-13}	1.18
PL-107C	nom / Tt2	whole rock	**16.25 ± 0.26**	5.020	4.096	9.626×10^{-11}	80.7
PL-162	14 / Ttd2	whole rock	**16.38 ± 0.26**	3.147	5.269	1.248×10^{-10}	85.9

Samples not within map area indicated as nom.

Table 3: Representative Chemical Analyses of Map Units

Sample	PL-193	PL-47B	PL-69	AW09-07	AW09-05	PL-41C	SP04-48	PL-107C	AW09-04	SP04-04	SP04-08	PL-79	PL-65	SP04-36
Map #	1	2	3	4	5	6	nom	nom	7	8	9	10	22	23
Map Unit	Qb	Qb	Qb	Qb	Qb	Qb	Tt1	Tt2	Tt2	Tt3	Tt3	Ttd1	Tr1	Tr1
NLat(27)°	42.1299	42.1582	42.1779	42.1105	42.1532	42.1445	42.1202	42.2749	42.2038	42.0594	42.0686	42.1919	42.1669	42.1407
WLong(27)°	119.1120	119.0846	119.0644	119.1123	119.0497	119.0845	119.1325	118.9570	119.0372	119.0346	119.0441	119.0375	119.0600	119.0259
SiO_2 (wt%)	47.51	47.58	47.98	48.19	48.40	48.64	63.91	63.59	64.12	64.25	64.41	68.64	72.01	72.11
TiO_2	1.00	0.93	0.92	0.96	0.99	0.98	1.04	0.96	0.94	0.84	0.82	0.63	0.42	0.36
Al_2O_3	17.17	16.95	17.21	17.16	16.72	16.66	16.63	16.12	16.12	16.13	15.73	15.63	14.88	14.61
Fe_2O_3	3.63	3.66	3.46	3.53	3.43	3.52	2.66	2.96	2.75	2.50	2.52	1.82	1.43	1.35
FeO	7.27	7.21	7.05	7.09	6.68	6.88	2.48	2.77	2.49	2.24	2.20	1.51	1.13	1.04
MnO	0.19	0.18	0.18	0.19	0.18	0.18	0.08	0.10	0.11	0.13	0.12	0.11	0.04	0.07
MgO	9.22	9.35	9.52	8.74	8.47	8.64	0.95	1.61	1.41	1.58	1.69	0.38	0.16	0.26
CaO	10.96	10.99	10.92	11.27	12.07	11.44	3.52	3.19	3.17	3.35	3.26	1.87	0.84	1.10
Na_2O	2.63	2.81	2.39	2.55	2.67	2.67	4.59	4.40	4.32	4.27	3.67	4.56	4.20	4.43
K_2O	0.25	0.23	0.24	0.21	0.23	0.23	3.70	3.99	4.24	4.42	5.32	4.65	4.84	4.56
P_2O_5	0.16	0.11	0.13	0.10	0.16	0.16	0.45	0.32	0.33	0.29	0.27	0.20	0.03	0.13
Total	99.98	100.01	100.04	99.79	100.76	100.06	99.31	98.85	99.57	99.25	98.94	96.86	97.46	98.85
Rb (ppm)	6	13	13	7	5	7	103	148	109	117	121	141	167	182
Sr	252	241	255	196	226	213	418	323	306	287	258	224	100	147
Ba	134	120	139	166	110	143	1173	954	1026	1034	1024	1040	585	723
Zr	78	80	85	55	61	55	278	350	326	342	333	313	268	235
Nb	nd	nd	nd	nd	nd	nd	15	nd	8	16	16	17	29	37
Y	25	30	31	24	24	23	41	61	30	43	34	40	40	24
Zn	nd	nd	nd	71	74	65	75	nd	87	75	64	78	51	56
Ni	148	155	156	133	123	114	4	10	27	14	11	18	13	5
V	265	254	236	231	257	245	64	92	97	92	82	25	18	22
Sc	nd	nd	nd	34	37	36	11	nd	12	12	11	7	6	4

Sample	PL-79B	SP04-42	PL-76B	PL-50C	PL-136	SP04-40	PL-128	SP04-46	SP04-25	SP04-22	AW09-15	PL-191	PL-113	PL-100
Map #	10	24	25	26	nom	nom	27	28	nom	29	nom	11	12	13
Map Unit	Tr1	Tr1	Tr1	Tr1	Tr2	Tr2	Tr2	Tr3	Tr3	Tr3	Ttd1	Ttd2	Ttd2	Ttd2
NLat(27)°	42.1919	42.1330	42.1902	42.1651	42.1443	42.1363	42.1390	42.0941	42.1039	42.0947	42.1635	42.0942	42.1357	42.1173
WLong(27)°	119.0375	119.0974	119.0610	119.0834	118.9742	118.9181	119.0048	119.1020	119.1320	119.1137	118.9992	119.0360	119.0110	119.0186
SiO_2 (wt%)	72.61	73.24	73.70	74.11	72.04	72.99	73.97	71.92	72.14	72.24	68.92	68.74	68.87	68.92
TiO_2	0.33	0.27	0.25	0.21	0.34	0.29	0.23	0.34	0.33	0.31	0.60	0.53	0.56	0.56
Al_2O_3	14.24	14.92	14.04	13.52	14.93	14.48	13.80	14.87	14.62	14.37	15.38	16.92	15.93	15.80
Fe_2O_3	1.22	0.95	1.05	0.95	1.19	1.18	1.14	1.25	1.16	1.19	1.73	1.63	1.63	1.67
FeO	0.95	0.77	0.80	0.73	0.86	0.85	0.80	0.87	0.78	0.78	1.45	1.24	1.23	1.28
MnO	0.04	0.03	0.06	0.04	0.05	0.08	0.04	0.07	0.07	0.06	0.07	0.06	0.05	0.06
MgO	0.24	0.15	0.13	0.11	0.06	0.07	0.03	0.06	0.11	0.06	0.60	0.17	0.25	0.22
CaO	1.18	0.68	0.85	1.13	0.48	0.26	0.33	0.40	0.44	0.40	1.96	0.73	1.10	1.22
Na_2O	4.34	3.74	3.51	4.17	4.61	4.41	4.44	4.76	4.72	4.69	4.11	4.54	4.74	4.69
K_2O	4.73	5.19	5.56	4.87	5.37	5.32	5.20	5.39	5.53	5.86	4.99	5.40	5.40	5.37
P_2O_5	0.12	0.07	0.05	0.17	0.07	0.07	0.03	0.06	0.09	0.04	0.19	0.02	0.24	0.20
Total	97.52	95.76	97.94	97.08	97.76	98.32	99.07	98.73	99.62	99.33	96.87	98.07	97.91	97.04
Rb (ppm)	174	172	200	169	167	184	188	169	164	169	148	130	146	148
Sr	118	73	94	70	47	21	15	26	28	27	202	114	181	174
Ba	530	652	500	364	595	281	135	430	533	425	842	1052	1395	1375
Zr	224	241	238	213	390	404	397	391	383	377	294	430	408	397
Nb	23	23	nd	25	25	28	30	25	26	25	27	nd	22	21
Y	30	26	44	31	47	42	43	47	58	47	34	23	28	31
Zn	48	37	nd	82	66	65	64	63	75	64	52	nd	55	60
Ni	12	2	3	11	1	<1	1	1	1	<1	17	3	3	2
V	19	14	5	5	16	8	10	17	14	14	25	10	28	29
Sc	5	nd	5	5	5	4	6	6	7	**7**	7	nd	7	8

Sample	PL-162	SP04-20	PL-63	SP04-33	AW09-06	SP04-10	AW09-14	AW09-16	SP04-45	SP04-29	SP04-32	SP04-43	SP04-03	SP04-01
Map #	14	15	16	17	18	19	20	21	30	31	32	33	34	35
Map Unit	Ttd2	Ttd2	Ttd2	Ttd2	Tr1	Tr1	Tr1	Tr1	Tr4	Tr4	Tr4	Tr4	Tr4	Tr4
NLat(27)°	42.1131	42.1213	42.1125	42.1257	42.1853	42.1683	42.1659	42.1607	42.0902	42.0772	42.0742	42.1247	42.0576	42.0668
WLong(27)°	119.0015	119.0099	119.0387	119.0498	119.0812	119.0846	119.0081	119.0134	119.0953	119.0768	119.1203	119.1046	119.0324	119.0307
SiO_2 (wt%)	68.99	69.15	69.47	70.02	70.39	71.22	71.67	71.93	71.89	73.05	73.11	73.88	74.52	74.95
TiO_2	0.55	0.52	0.50	0.43	0.48	0.39	0.39	0.42	0.33	0.26	0.21	0.22	0.17	0.18
Al_2O_3	15.93	16.60	15.62	15.80	14.86	14.33	14.57	14.98	14.73	14.18	15.43	13.72	13.54	13.43
Fe_2O_3	1.61	1.56	1.50	1.33	1.50	1.41	1.34	1.52	1.30	1.03	1.12	1.11	0.93	0.71
FeO	1.23	1.23	1.12	0.99	1.27	1.11	1.03	1.22	0.94	0.75	0.97	0.76	0.62	0.46
MnO	0.06	0.04	0.05	0.07	0.09	0.08	0.06	0.03	0.08	0.10	0.09	0.07	0.08	0.02
MgO	0.28	0.18	0.22	0.20	0.62	0.53	0.24	0.16	0.18	0.12	0.14	0.06	0.04	0.02
CaO	1.19	0.69	0.96	0.89	1.64	1.45	1.36	0.76	0.69	0.56	0.44	0.18	0.16	0.11
Na_2O	4.68	4.15	4.65	4.65	3.92	3.54	4.41	4.03	4.70	4.05	3.24	4.45	4.87	4.75
K_2O	5.26	5.84	5.51	5.49	5.03	5.80	4.70	4.92	5.06	5.83	5.17	5.48	5.06	5.35
P_2O_5	0.22	0.04	0.39	0.13	0.18	0.14	0.23	0.03	0.09	0.06	0.07	0.07	0.01	0.01
Total	97.64	95.96	97.53	97.65	95.60	97.08	98.53	97.15	98.80	97.40	94.44	98.69	100.20	99.91
Rb (ppm)	151	153	150	153	167	172	165	159	163	179	178	195	203	211
Sr	158	120	138	113	165	159	150	100	69	46	20	9	11	10
Ba	1185	1197	1240	1151	749	886	890	613	707	530	194	122	118	106
Zr	421	377	405	373	292	247	265	260	335	304	372	379	345	363
Nb	22	22	22	22	24	31	23	29	25	28	36	31	33	33
Y	36	32	26	36	37	33	39	30	46	47	98	85	54	66
Zn	57	54	49	50	58	52	57	51	58	73	89	76	68	92
Ni	2	3	2	2	11	1	10	12	1	<1	<1	<1	1	2
V	30	26	25	22	27	28	18	25	14	8	9	11	7	4
Sc	8	7	7	7	8	6	4	6	5	5	6	4	3	6

Sample	SP04-07	PL-184B	SP04-50	AW09-12	SP04-06
Map #	36	37	nom	nom	38
Map Unit	Tr5	Twt1	Twt1	Twt1	Twt2
NLat(27)°	42.0656	42.0898	42.1167	42.0701	42.0650
WLong(27)°	119.0443	119.1116	119.1477	119.2437	119.0454
SiO_2 (wt%)	72.26	75.09	75.85	76.52	71.74
TiO_2	0.33	0.17	0.21	0.19	0.35
Al_2O_3	14.50	13.24	12.19	11.93	14.79
Fe_2O_3	1.14	1.08	1.24	1.15	1.13
FeO	0.79	0.75	0.85	0.82	0.83
MnO	0.07	0.06	0.07	0.07	0.10
MgO	0.20	0.00	0.09	0.07	0.25
CaO	0.70	0.13	0.03	0.09	0.81
Na_2O	4.59	4.48	4.38	4.35	4.17
K_2O	5.39	4.96	5.02	4.78	5.76
P_2O_5	0.03	0.02	0.07	0.02	0.06
Total	99.45	99.30	99.52	98.42	97.67
Rb (ppm)	177	223	188	194	182
Sr	63	11	10	8	67
Ba	463	234	137	47	492
Zr	295	395	470	472	291
Nb	26	nd	27	19	25
Y	47	42	47	51	45
Zn	51	nd	84	82	61
Ni	<1	3	<1	2	<1
V	17	<2	7	<2	15
Sc	nd	6	6	7	

Major element data in weight (wt) % and trace element data in parts per million (ppm); major element data reported as 100% anhydrous after conversion of total Fe to FeO and Fe2O3 (LeMaitre, 1976) with pre-normalization total reported. Locations quoted for NAD27 datum. Abbreviations for samples not located within map boundary (nom) and element concentrations not determined (nd).

Silicic Units of Lone Mountain

Lone Mountain rhyolite

The Lone Mountain rhyolite (71.4-74.6 wt% SiO_2) underlies the Lone Mountain trachydacite in the central and eastern portions of Lone Mountain extending well off of the map area to the north and northeast. Exposures in stream cuts indicate a minimum thickness 50 m. Both upper and lower flow vitrophyres are observed and frothy, pumiceous upper flow material is locally preserved. Flow lobes/fronts of the Funnel Canyon rhyolite and the Lone Mountain rhyolite are juxtaposed in undetermined stratigraphic contexts along the north-northwest flank of Lone Mountain. Field distinction between these rhyolites is difficult, but chemical differences are notable (Table 3).

The Lone Mountain rhyolite is light to dark gray with hues of pink and blue on freshly exposed surfaces and is visibly flow banded. Weathered surfaces are tan with clay filling in cavities. In thin section this unit is sparsely porphyritic with a cryptocrystalline, banded spherulitic groundmass. Phenocrysts include sanidine, plagioclase, clinopyroxene, and biotite. Feldspars often display disequilibrium textures, with sanidine up to 5 mm and plagioclase up to 1.25 mm in length. The Lone Mountain rhyolite generally can be distinguished from other silicic units by a combination of being matrix-dominated (>80%) and devoid of anorthoclase.

Lone Mountain trachydacite: 16.4 ± 0.2 Ma

The Lone Mountain trachydacite (68.5-70.0 wt% SiO_2) is exposed throughout the southwestern portion of Lone Mountain and is interpreted as remnants of a large silicic dome core with surrounding outflow (Figure 5A and B). The aggregate unit thickness is estimated to be up to 330 meters. The dome core itself is extensively exfoliated and heavily jointed and displays distinctive weathering patterns of rounded pinnacles and jagged forms not observed elsewhere the map area (Figure 5B). This trachydacite is light gray on fresh surface and weathers from white to yellow-brown. Flows emanating from the core have a darker matrix, ranging from dark gray to black, weather to a deep red color, and erode more sharply than the exfoliated core. Prominent flow features are visible on outcrop scale with individual flow units up to 20-50 m thick. Upper and lower flow vitrophyres are common. Some vertical to near-vertical flow patterns are locally observed that may represent feeder localities. These features vary from small discontinuous dikes (5 m high, 30 m in length along the margin of the dome) to a volcanic plug (25 m high, 20 m in length in the central part of the dome). Contacts between the dome core and flows emanating from this core are based on the presence or absence of flow features, rock color and weathering pattern.

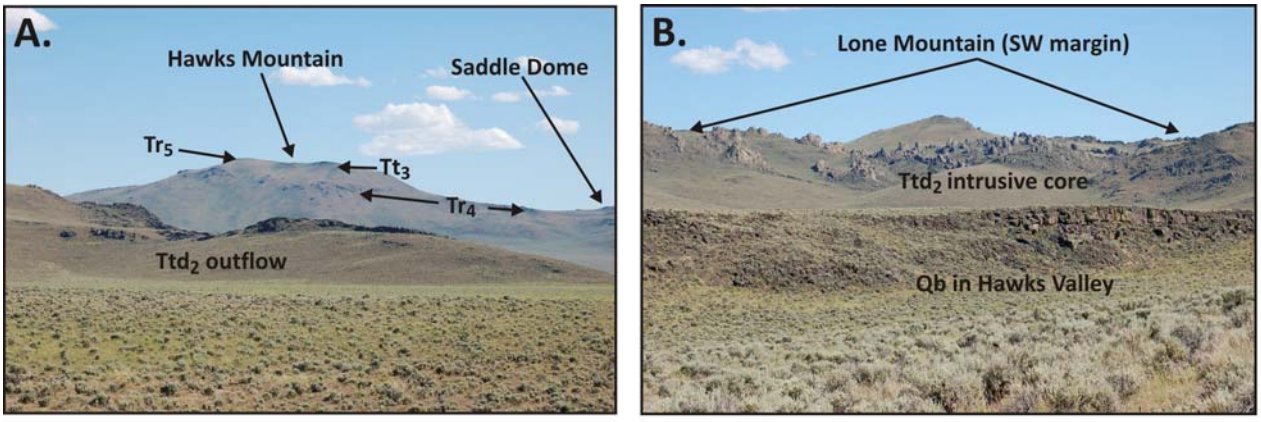

Figure 5: Photograph from HVLM project (A) South across SW margin of Lone Mountain to southern faulted margin (Mio-Pliocene NW-striking fault) of Hawks Valley at Hawks Mountain; (B) From southern end of Funnel Canyon over small displacement ~N-S fault in Qb into highly jointed Lone Mountain core trachydacite (Ttd_2).

In thin section this unit displays slight flow banding and a cryptocrystalline to glassy matrix with phenocrysts of anorthoclase, sanidine, plagioclase, biotite, and clinopyroxene. Most crystals are anhedral, with anorthoclase and sanidine ranging up to 4 mm and plagioclase up to 5.5 mm in length, all commonly displaying disequlibrium features (Figure 6A). The biotite and clinopyroxene are altered to chlorite/clay/oxide. Feldspars from two separate glassy samples yield Ar-Ar ages of 16.40 ± 0.19 and 16.46 ± 0.21 Ma and a whole rock K-Ar determination yields an age of 16.38 ± 0.26 Ma (Tables 1and2).

Silicic Units of Funnel Canyon

Funnel Canyon trachydacite

The Funnel Canyon trachydacite (68.6-68.9 wt% SiO_2) has been identified in only one location within the map area, along the southern-most main fault bounding the eastern side of Funnel Canyon. Here the unit conformably underlies the Funnel Canyon rhyolite. Additional exposures and a possible vent locality are observed just east of the northeastern portion of the map area. Based on these exposures a minimum unit thickness of 60 m is estimated. This trachydacite is gray on fresh surface and weathers to yellow-brown. Flow banding is visible in outcrop and in thin section where it is accentuated by the alignment of crystals. The unit is porphyritic with a cryptocrystalline to glassy matrix and anhedral phenocrysts (2-5 mm) of sanidine, plagioclase, clinopyroxene and biotite.

Funnel Canyon rhyolite: 16.5 ± 0.3 Ma

The Funnel Canyon rhyolite (70.4-74.4 wt% SiO_2) crops out extensively along the northwest flank of Lone Mountain and dominates the exposures throughout the southern portion of Funnel Canyon. At least three chemically distinct flow units are identified, but these are indistinguishable in field appearance hence are not separately indicated on the map. Numerous N-NE trending fault scarps in Funnel Canyon reveal individual flow unit thicknesses of at least 30 m and an aggregate thickness of no less than 300 m. The upper flow margins are characterized by porphyritic vitrophyre. This unit is light to dark

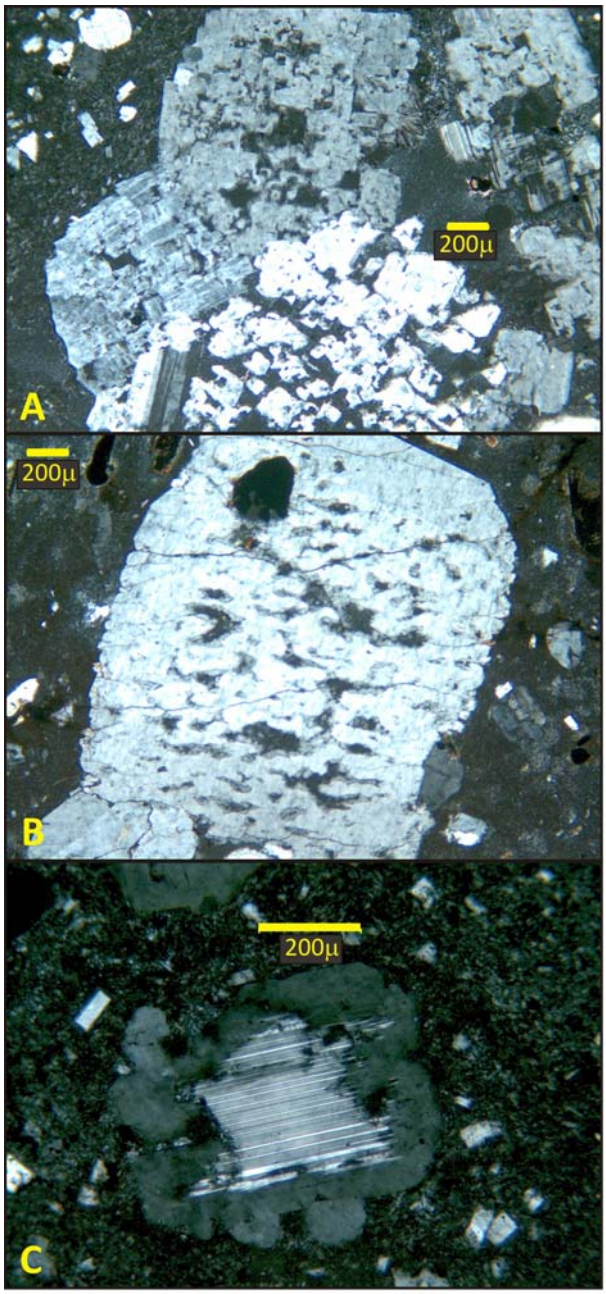

Figure 6: Photomicrographs of selected HVLM silicic units (scale bars are 200 microns) displaying evidence for complex crystallization histories including open system processes. (A) alkali feldspar and plagioclase phenocrysts with partially resorbed cores from the Lone Mountain trachydacite (Ttd_2); (B) plagioclase feldspar from the Saddle Dome rhyolite (Tr_4) displaying a sieved core; (C) feldspar from the Saddle Dome rhyolite showing a two-stage growth history with initial plagioclase feldspar (xenocryst?) that was partially resorbed and alkali feldspar, itself with embayed edges, later growing around the resorbed and embayed margins of the plagioclase.

gray on fresh surface with some color variations of pink and tan, and weathers red to black. Outcrops and hand samples display pronounced wavy to contorted flow banding. The eastern contact relationships with Lone Mountain are stratigraphically ambiguous. Two vents are identified as remnant lava domes along the southwestern edge of the main Funnel Canyon rhyolite and on the up-thrown side of the young Hawks Valley fault ("Scarp Dome"; Figure 7A and B). Two additional possible vent localities are observed in Funnel Canyon where brecciated oxidized vitrophyre caps intensely contorted, vertically flow banded rhyolite (Figure 7C).

In thin section the Funnel Canyon rhyolite is porphyritic to glomeroporphyritic with a cryptocrystalline to fresh glassy matrix. Flow banding is evident as alternating bands of decreased glass and increased broken crystals. Phenocrysts include sanidine, plagioclase, orthopyroxene, biotite, and clinopyroxene. Feldspars are subhedral to anhedral often displaying disequilibrium features and are up 3.5 mm in length, and smaller mafic crystals often are altered to chlorite. Feldspars from a vitrophyre yielded an Ar-Ar age of 16.51 ± 0.25 Ma (Table 1).

Basque Hills trachyte: 16.3 ± 0.3 Ma

The Basque Hills trachyte (62.9-64.1 wt% SiO_2) crops out in the northeastern portion of the map area in and adjacent to Funnel Canyon, to the N-NW of this throughout the Basque Hills, along the southeastern flank of Lone Mountain, and well to the east of the map area along the western flank of the Pueblo Mountains, and is estimated to possess a minimum thickness of 15 m. Along the western edge of Funnel Canyon this trachyte appears to overlie the Funnel Canyon rhyolite. Two possible vent areas are inferred; in the northeastern corner of the map area and outside the map area at the northeastern terminus of Funnel Canyon. Outcrops are typically massive with flattened vesicles at the top to platy at the base. In hand sample the Basque Hills trachyte is black and very fine grained with prominent feldspar crystals, and easily can be mistaken for

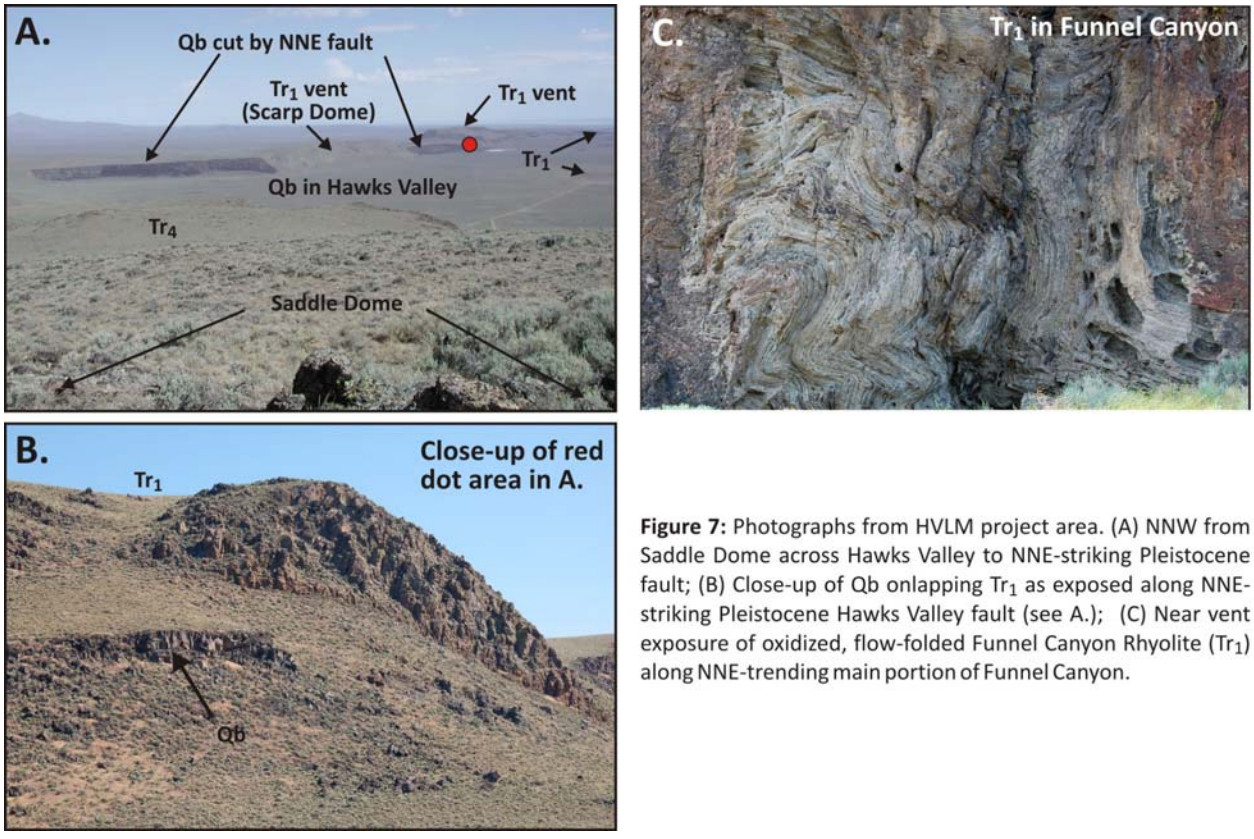

Figure 7: Photographs from HVLM project area. (A) NNW from Saddle Dome across Hawks Valley to NNE-striking Pleistocene fault; (B) Close-up of Qb onlapping Tr_1 as exposed along NNE-striking Pleistocene Hawks Valley fault (see A.); (C) Near vent exposure of oxidized, flow-folded Funnel Canyon Rhyolite (Tr_1) along NNE-trending main portion of Funnel Canyon.

basalt. In thin section it displays a very fine pilotaxitic feldspar-glass matrix with plagioclase, orthopyroxene, and clinopyroxene. Plagioclase crystals are up to 5 mm and often are resorbed to skeletal with normal and oscillatory zoning. This unit is readily distinguished from most others by the lack of alkali feldspar phenocrysts and by pilotaxitic plagioclase aligned with flattened vesicles. A whole rock aliquot of the trachyte yielded a K-Ar age of 16.25 ± 0.26 Ma (Table 2).

Silicic Units of the Acty Mountain – Hawks Mountain Region

Bald Mountain trachyte

The Bald Mountain trachyte (~64 wt% SiO_2) is prominently exposed to the west of the map area along the northern flank of Bald Mountain and projects into the map area in the Acty Mountain region where it is up to 60 m thick and observed to uncomfortably underlie the Acty Mountain rhyolite. In hand sample the rock is gray to black, massive and fine-grained, with identifiable flow banding accentuated by weathering. Microphenocrysts of plagioclase, orthopyroxene, clinopyroxene and iron-titanium oxide are most obvious in thin section but visible in hand sample.

Acty Mountain rhyolite: 16.4 ± 0.2

The Acty Mountain rhyolite (71.0-72.2 wt% SiO_2) is found only proximal to Acty Mountain achieving an estimated aggregate thickness of 180 m. Individual exposures up to 25 m thick exhibiting 5-10° S-SE dips away from the Acty Mountain summit region suggest an eruptive locality just to the west of the map area. This unit displays well developed flow banding, typically is pervasively oxidized with a thick weathering rind, and locally preserves zones of vitrophyre. Fresh surfaces expose a light gray to light purple hypocrystalline matrix with feldspar crystals.

In thin section this rhyolite is porphyritic with a cryptocrystalline to glassy groundmass showing contorted flow banding. Phenocrysts include sanidine (up to 3 mm), fayalitic olivine (up to 1 mm), clinopyroxene, and biotite; many sanidine crystals display disequilibrium textures. Feldspars from a vitrophyre yielded an Ar-Ar age of 16.39 ± 0.17 Ma. While this age is indistinguishable within analytical error from that determined for the Saddle Dome rhyolite, it is in agreement with field observations that place the Saddle Dome rhyolite stratigraphically above the Acty Mountain rhyolite.

Saddle Dome rhyolite: 16.3 ± 0.2

The Saddle Dome rhyolite (71.9-75.3 wt% SiO_2) completely surrounds Hawks Mountain extending as far southeast as Lone Juniper, and is continuously exposed to the southwest of the main NW-trending Hawks Valley fault scarp in a topographic saddle between Acty Mountain and Hawks Mountain (Figure 5A). The Saddle Dome rhyolite represents multiple flow units with an estimated aggregate thickness of at least 300 m, displays a characteristic gray to purple color with visible dark flow banding, and locally preserves thick upper vitrophyre and frothy, pumiceous flow top. Distinct large flow lobes are discerned and point to a possible central eruptive locality between Acty and Hawks Mountains ("Saddle Dome").

In thin section this rhyolite displays fine-grained feldspar dominated or devitrified glass matrix hosting crystals of predominantly plagioclase, anorthoclase, and sanidine up to 4.5 mm in size, all frequently displaying disequilibrium textures (Figure 6B and C). Thus, while the unit has a porphyritic texture, in some samples there can be as much as 95% matrix and only 5% crystals. Iron-titanium oxides, biotite, and clinopyroxene are ubiquitous microphenocrysts. Feldspars from a Saddle Dome rhyolite vitrophyre yielded an Ar-Ar age of 16.33 ± 0.17 Ma.

Hawks Mountain trachyte

The Hawks Mountain trachyte (64.3-65.2 wt% SiO_2) is observed only near the top of Hawks Mountain where it is no thicker than 150 m and stratigraphically overlies the Saddle Dome rhyolite (Figure 5A). The upper portion of the trachyte weathers into plates that display a very fine grained gray to black matrix containing clinopyroxene and orthopyroxene phenocrysts up to 2 mm and abundant plagioclase phenocrysts up to 5 mm. In thin section these phenocrysts and glomeroporphyritic clusters of plagioclase and

pyroxene are set in a hypocrystalline matrix containing numerous flow aligned plagioclase laths providing a trachytic texture. Inclusions of smaller plagioclase or pyroxene crystals inside the larger plagioclases are not uncommon and many plagioclase crystals display oscillatory zoning and resorbed cores. Although no source vent has been firmly established, the outcrop pattern is consistent with a source proximal to or just to the southeast of Hawks Mountain.

Hawks Mountain rhyolite

The Hawks Mountain rhyolite (~72 wt% SiO_2) is restricted to the present-day summit area of Hawks Mountain where it conformably overlies the Hawks Mountain trachyte (Figure 5A). This unit typically is platy and flow banded with a gray to purple matrix hosting feldspar phenocrysts and visible biotite. This rhyolite is compositionally difficult to distinguish from the Saddle Dome rhyolite, but stratigraphic relationships require formal distinction. In thin section the rhyolite displays a fine-grained feldspar dominated, hypocrystalline groundmass with plagioclase and sanidine phenocrysts up to 2.5 mm and scattered biotite and oxide. Many of the feldspars possess sieve textures and are broken or incomplete. Although no source vent has been established, the outcrop pattern is consistent with a source proximal to Hawks Mountain.

Idaho Canyon Tuff/Oregon Canyon Tuff: 16.3 ± 0.2

Two separate ash-flow tuff units (Twt_1 and Twt_2) are identified and mapped along the southern portions of the HVLM project area where locally they are juxtaposed in an uncertain stratigraphic relationship. Twt_1 is widely exposed to the west, south and southwest of Acty Mountain extending for at least 20-25 km to Oregon/Nevada Highway 291/140 and beyond, reaching minimum local thicknesses in excess of 25 meters. Isolated ~5 m thick patches of deep red weathered Twt_1 are exposed on top of the NE-trending Hawks Valley fault scarp, locally overlying the Funnel Canyon rhyolite. Twt_1 appears to on-lap the lava flow materials comprising the high regions from Hawks Mountain to Acty Mountain, thus may represent among the youngest silicic materials in the map area. Fresh surfaces are gray to pink with ovoid to flattened black fiamme that when weathered provide a “swiss cheese” appearance. Locally this unit displays prominent zones of ovoid lithophysae up to 15 cm in long dimension. Minor crystals of sanidine and oxides and sparse intermediate to mafic lithic fragments are set in an intensely welded glassy groundmass displaying secondary flowage with aligned and variably devitrified fiamme. The wide inferred distribution, intense welding, and rheomorphic features suggest emplacement as a high-temperature ash-flow sheet(s).

Twt_2 also appears to on-lap the lava flow material comprising the southwestern side of Hawks Mountain with more extensive exposures extending to the south of the map area. Clear stratigraphic relationships between Twt_1 and Twt_2 are not observed within or adjacent to the map area. Within the map area outcrops of this unit are up to 20 m thick and weather into spires. The unit is readily distinguished from Twt_1 by being crystal rich with 2 to 4 mm feldspar set in a dark gray to black dense, fine-grained matrix. Tan pumice up to 1 cm in size also is common. In thin section sanidine, plagioclase, biotite, and pyroxene phenocrysts are observed in a glassy, devitrifying matrix. Feldspars are up to 3 mm in size and commonly are step-zoned or display partially resorbed edges and a cellular texture. Biotite and pyroxenes occur in minor amounts with pyroxene commonly preserving compositional zonation.

Both Twt_1 and Twt_2 appear to have flowed approximately northward from an eruptive location(s) well to the south of the HVLM. The aerial extent, petrography, and chemistry suggest that Twt_1 and Twt_2 are correlative with the Idaho Canyon Tuff/Oregon Canyon Tuff (Walker and McLeod, 1991; Rytuba and McKee, 1984; Green, 1984; Colgan et al., 2006; Henry et al., 2006; Lerch et al., 2008; C. Henry and M. Coble, personal communication, 2010). Based on this link and using the same Ar calculation parameters employed in this study, an age of 16.3 ± 0.2 is

inferred for these stratigraphic units (above references and Jarboe et al., 2010).

Quaternary Basalt

Tholeiitic basalts of Hawks Valley and Funnel Canyon: 0.5-0.8 Ma

Basalt (47.3-49.0 wt% SiO_2; 7.8-9.9 wt% MgO) is encountered throughout Hawks Valley, in southern Funnel Canyon, and across the northwestern portion of map area and is best exposed in the northeast trending fault scarp defining the western edge of Hawks Valley where multiple compound pahoehoe flow units ranging in thickness from 5-15 m are observed (Figure 7A and B and Figure 8). Local thinner, clastogenic flows and agglutinate are observed proximal to a remnant cone bisected by the NE-trending fault and an eruptive fissure along the base of the fault. A minimum aggregate thickness of 90 m is estimated.

These basalts are holocrystalline with plagioclase > augite > olivine > oxides and often contain phenocrysts and glomerocrysts of olivine and plagioclase. In addition, they are characteristically diktytaxitic and subophitic with intergranular oxide. The petrography and chemistry of this entire basalt package corresponds to the regionally important low-K, high-alumina olivine tholeiite (HAOT) basalt type defined by Hart et al. (1984). Two whole rock K-Ar age determinations (0.47 ± 0.23, fault scarp and 0.81 ± 0.25, Funnel Canyon) constrain this unit to the Pleistocene.

Figure 8: Photograph of stacked flows/lobes of Pleistocene tholeiitic basalt (Qb) exposed along post-basalt emplacement NNE-striking Hawks Valley fault.

PETROLOGY AND GEOCHEMISTRY

The bulk chemical characteristics of HVLM volcanic rocks define four primary compositional groups; basalt, trachyte, trachydacite, and rhyolite (Figures 9A and B, Table 3). The Quaternary basalts define a very tight cluster on Figure 9A highlighting the limited chemical variations observed within this stratigraphic unit (Table 3). Clearly the young HVLM basalts, and in a regional sense HAOT as a magma type, help to define the least differentiated end of the HLP-ION area late Cenozoic basalt compositional spectrum. The higher silica end of the HVLM eruptive products displays greater compositional diversity and complexity, in agreement with the petrographic characteristics previously described, including the evidence for open system magmatic processes illustrated in Figure 6. From the nomenclature standpoint, the distinction between the trachytes, trachydacites, and rhyolites is drawn from a combination of total alkali, silica, and normative quartz and feldspar contents (Figures 9A and B). The vast majority of the silica-rich units are peraluminous or metaluninious, with only some samples of the ash-flow tuffs (Twt_1 and Twt_2), the Saddle Dome rhyolite, and the Acty Mountain rhyolite displaying mildly peralkaline signatures (Figure 9C). These traits support our interpretation that the ash-flow units are correlative with the Idaho/Oregon Canyon Tuff (Rytuba and McKee, 1984, C. Henry and M. Coble, personal communication, 2010).

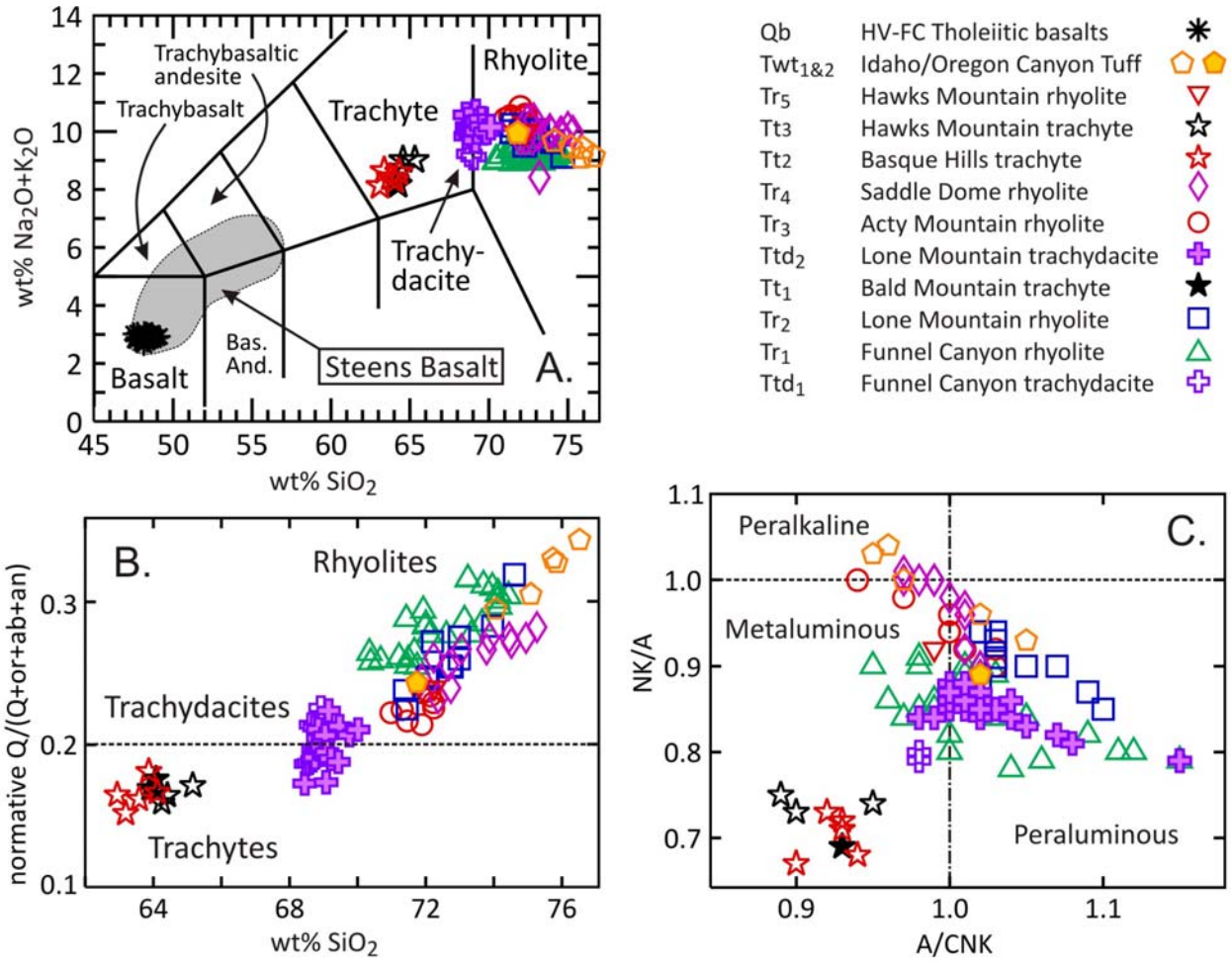

Figure 9: Classification and nomenclature plots. (A) Total alkali versus silica diagram after Le Bas et al., (1986) with Steens Basalt field drawn using data from Brueseke et al. (2007) and references therein; (B) Distinction between trachyte and trachydacite based on normative quartz content; (C) Aluminum saturation diagram with molecular $[Na_2O+K_2O]/Al_2O_3$ (NK/A) versus $Al_2O_3/[CaO+Na_2O+K_2O]$(A/CNK). Prior to classification calculations and plotting, all of the data were recalculated to 100% anhydrous with Fe split into FeO and Fe_2O_3.

Selected major and trace element concentrations are plotted versus Sr concentration in the diagrams of Figure 10 in order to highlight geochemical differences and similarities between and within the trachyte through rhyolite stratigraphic units. Other element-element and element ratio plots provide similar relationships. A number of important relationships illustrated by Figure 10 bear mentioning. First, the Funnel Canyon (Tr_1) and Lone Mountain (Tr_2) Rhyolites are difficult to distinguish in the field, yet chemically they are quite distinct. Furthermore, the Lone Mountain rhyolite defines compositional arrays in multi-element space offset from all other rhyolite units and characterized by elevated Sr concentrations (~60-180 ppm) accompanied by lower Zr concentrations (≤310 ppm)(Figure 10). In comparison, other high-silica units are Sr-poor (~10-70 ppm) and more variable in Zr (~280-480 ppm). In addition, the Funnel Canyon rhyolite exhibits at least three chemical subsets: (1) a low Sr (~60-100 ppm), low Al_2O_3 (~13.5-14 wt%), and low Ba (~350-500 ppm) concentration subgroup; (2) a medium Sr (~100-110ppm), high Al_2O_3 (14.5-15.0 wt%), and medium Ba (~550-600 ppm) subgroup; and (3) a high Sr (~125-180 ppm), Al_2O_3 (~14.0-15.3 wt%), and Ba (~640-900 ppm) subgroup (Figure 10). The remaining rhyolite units (~71-77 wt% SiO_2) display broadly similar to

overlapping chemical characteristics and overall concentration ranges with important caveats: (1) Twt_1 extends to the highest silica concentration and displays heterogeneities indicative of variable juvenile and accidental crystal and lithic content; (2) the Saddle Dome rhyolite (Tr_4) appears to include two subgroups, one with higher Sr (~60 ppm), Ba (>400 ppm), and lower Zr (<350 ppm) than the other (Figure 10, Table 3).

and (3) the pronounced differences in Ba and Zr concentrations between the Lone Mountain and Funnel Canyon trachydacites.

The plots provided in Figure 10 also illustrate a number of linear and sub-linear arrays defined either by individual or multiple stratigraphic units. Most noteworthy are the three non-overlapping arrays with different slopes in SiO_2-Sr, TiO_2-Sr, and Ba-Sr space defined by the Lone Mountain

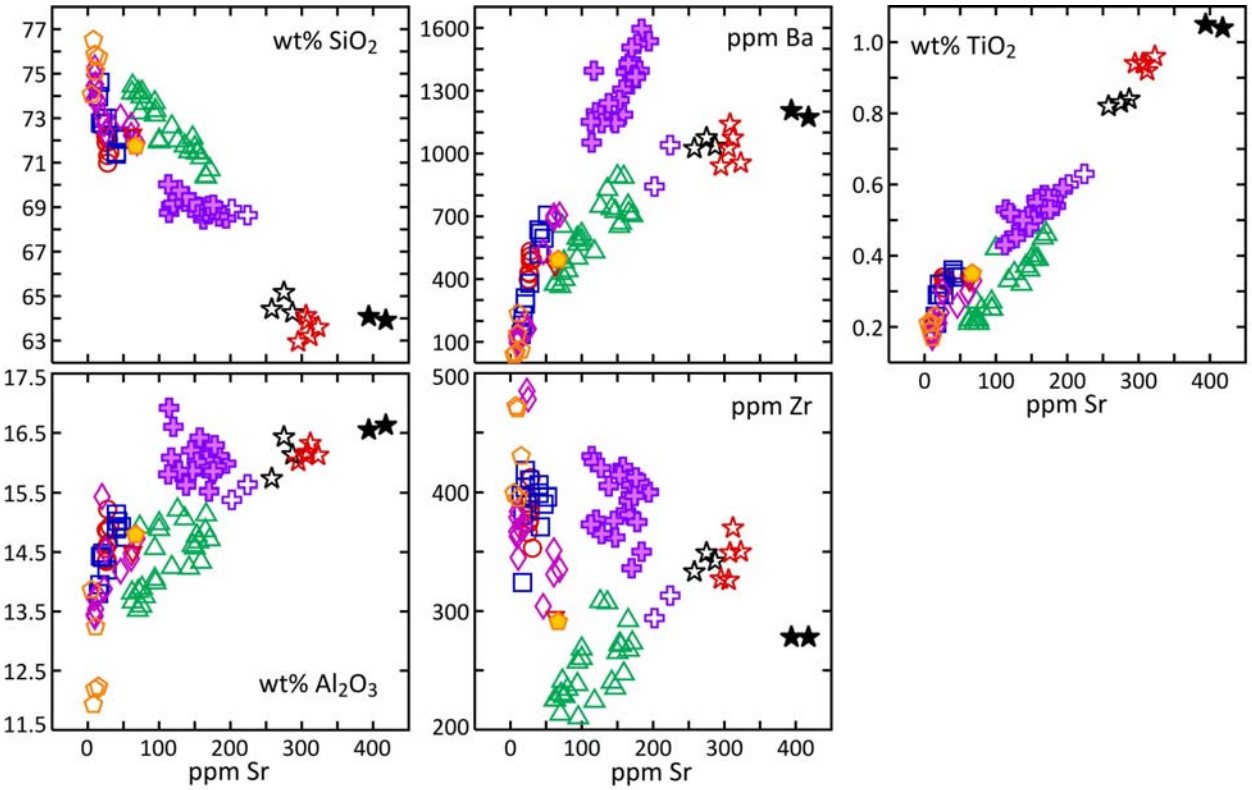

Figure 10: Major and trace element groups and variations for silicic units. Selected major elements and trace elements plotted versus Sr concentration to illustrate (1) the geochemical distinctions between the individual trachyte and trachydacite stratigraphic units; (2) the presence of subgroups within the Funnel Canyon rhyolite (green triangles); (3) the similar geochemical signatures of the other rhyolite units; (4) within-unit geochemical heterogeneity; and (5) linear trends indicative of crystal fractionation and/or mixing processes. Symbols as in previous figure.

The less evolved (~63-70 wt% SiO_2) trachyte and trachydacite stratigraphic units are readily distinguished in multi-element space as displayed in Figure 10. Particularly noteworthy are: (1) the clustering of the trachyte groups at elevated concentrations of Sr, TiO_2, Al_2O_3, and Ba; (2) the very distinct chemical characteristics of the Lone Mountain trachydacite (Ttd_2), particularly its elevated Ba concentrations (~1000-1600 ppm);

trachydacite, the Funnel Canyon rhyolite, and the majority of the other rhyolites. These three general groupings also are obvious in Zr-Sr space. The groupings and arrays defined in Figure 10 and discussed above provide first-order evidence for complex magma evolution processes including fractional crystallization, magma mixing, and assimilation-fractional crystallization (AFC), and for the likelihood that one or more of these

processes were acting on discrete batches of magma generated from heterogeneous mantle and crustal sources leading to multiple, separate magmatic systems beneath the HVLM.

Figures 11 and 12 are multi-element plots ("spider diagrams") for the HVLM silicic units. All individual element concentrations are normalized to an average total continental crust calculated by Rudnick and Fountain (1995). These plots reinforce the observations and assertions discussed above. Moreover, all of the rhyolites display relative depletions in Ba, Sr, and Ti and for all but the Acty Mountain rhyolite the within-unit depletions are highly variable (Figure 11). These characteristics require a major role for crystal fractionation of phases such as feldspar, pyroxene, and Fe-Ti oxide. Once again the Funnel Canyon rhyolite sets itself apart from all other silicic units. The multi-element plots in Figure 12 reinforce the previously noted distinctions between the trachyte and trachydacite units and the overall similarities of individual units within these two compositional groups. Compared to the rhyolites, these units display patterns indicative of lesser amounts of crystal fractionation and less within unit heterogeneity.

The geochemical data discussed above in combination with field and chronostratigraphic information, petrographic indicators of complex magma cooling histories and open system magmatic processes (e.g., Figure 6; complex feldspar textures) allow for first-order assessment of magma generation and evolution processes responsible for the mid-Miocene HVLM trachyte-trachydacite-rhyolite volcanism. Inherent in this assessment is the a-priori assumption that spatially and temporally associated Steens Basalt magmatism serves as a material and/or thermal driver for the silicic volcanism. Additional potential melt and/or contaminant reservoirs include upper crust, as represented by nearby Cretaceous granitoid materials and published averages, and lower crust, as represented by regional Early Miocene arc lavas and published averages. With these parameters in mind, Figure 13 displays three general scenarios that are forwarded as preliminary models to account for HVLM silicic unit diversity and petrogenesis: (1) crystal fractionation (FC) and assimilation and fractional crystallization (AFC) with mafic lower crust or underplated arc magmas; (2) assimilation and fractional crystallization (AFC) and mixing with lower to upper crustal melts and lithologies; and (3) crystal fractionation (FC), assimilation and fractional crystallization (AFC) and magma mixing in the middle to upper crust. It is clear from this qualitative modeling that no single process can explain the observed data. Moreover, the range of Steens Basalt chemical characteristics, which may have an origin in AFC processes, provides a variety of possible "parental" mafic to intermediate endmembers. Regardless of this and the diversity of possible crustal melts that could be generated, we suggest that differentiation from mafic and silicic parental magmas via fractional crystallization, AFC, and magma mixing (combination of models B and C in Figure 13) lead to the diversity of mid-Miocene silicic volcanism documented in the HVLM.

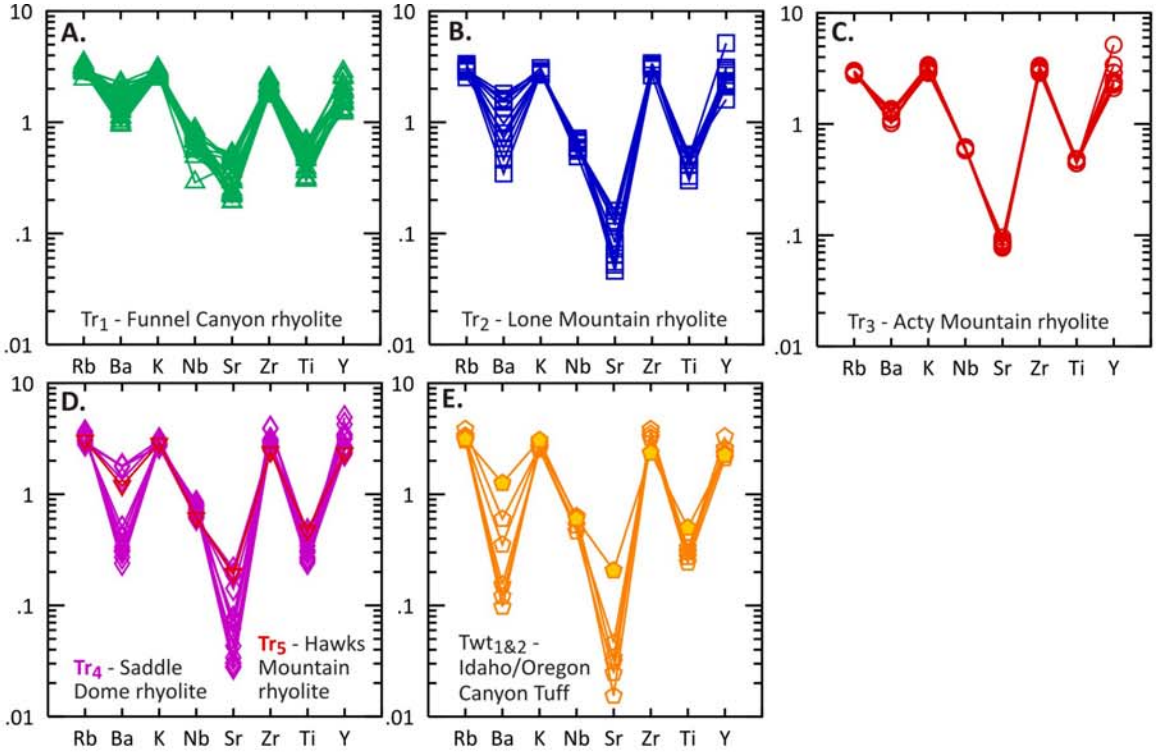

Figure 11: Rhyolite multi-element plots. Elements normalized to average total crust of Rudnick and Fountain (1995). (A) Funnel Canyon rhyolite; (B) Lone Mountain rhyolite; (C) Acty Mountain rhyolite; (D) Saddle Dome and Hawks Mountain rhyolites; (E) proposed correlatives to Idaho/Oregon Canyon Tuff.

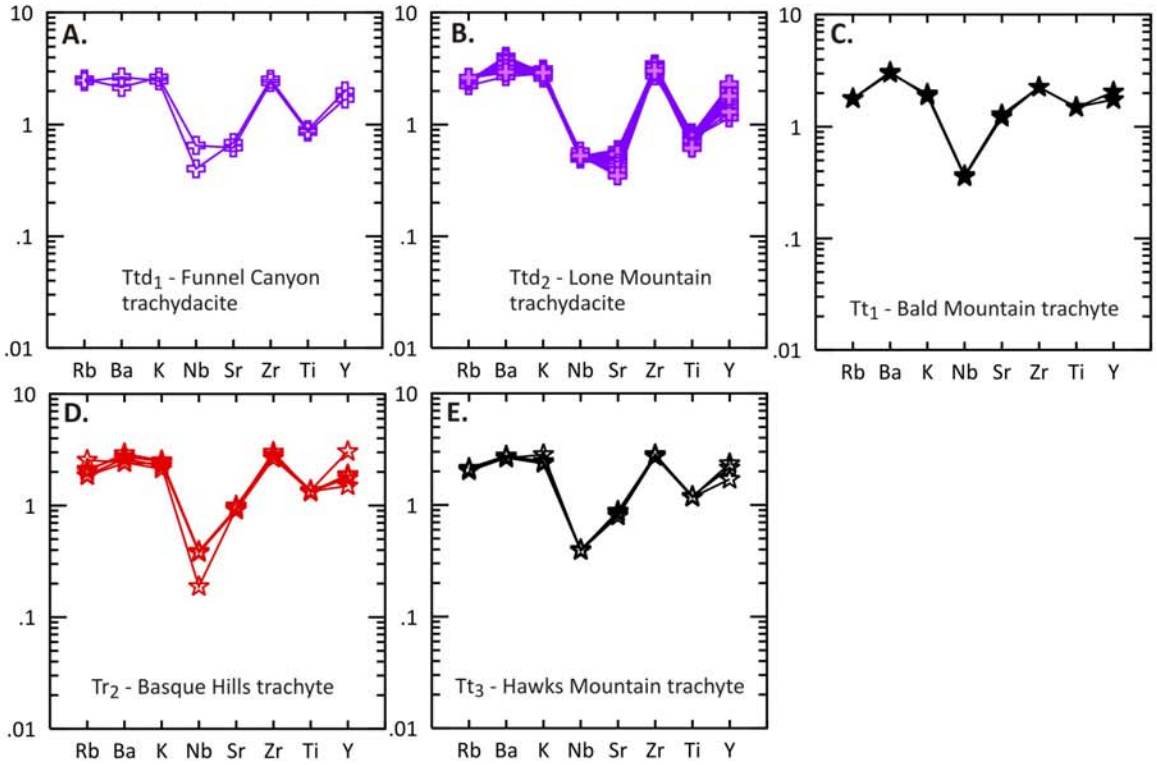

Figure 12: Trachyte and trachydacite multi-element plots. Elements normalized to average total crust of Rudnick and Fountain (1995). (A) Funnel Canyon trachydacite; (B) Lone Mountain trachydacite; (C) Bald Mountain trachyte; (D) Basque Hills trachyte; (E) Hawks Mountain trachyte.

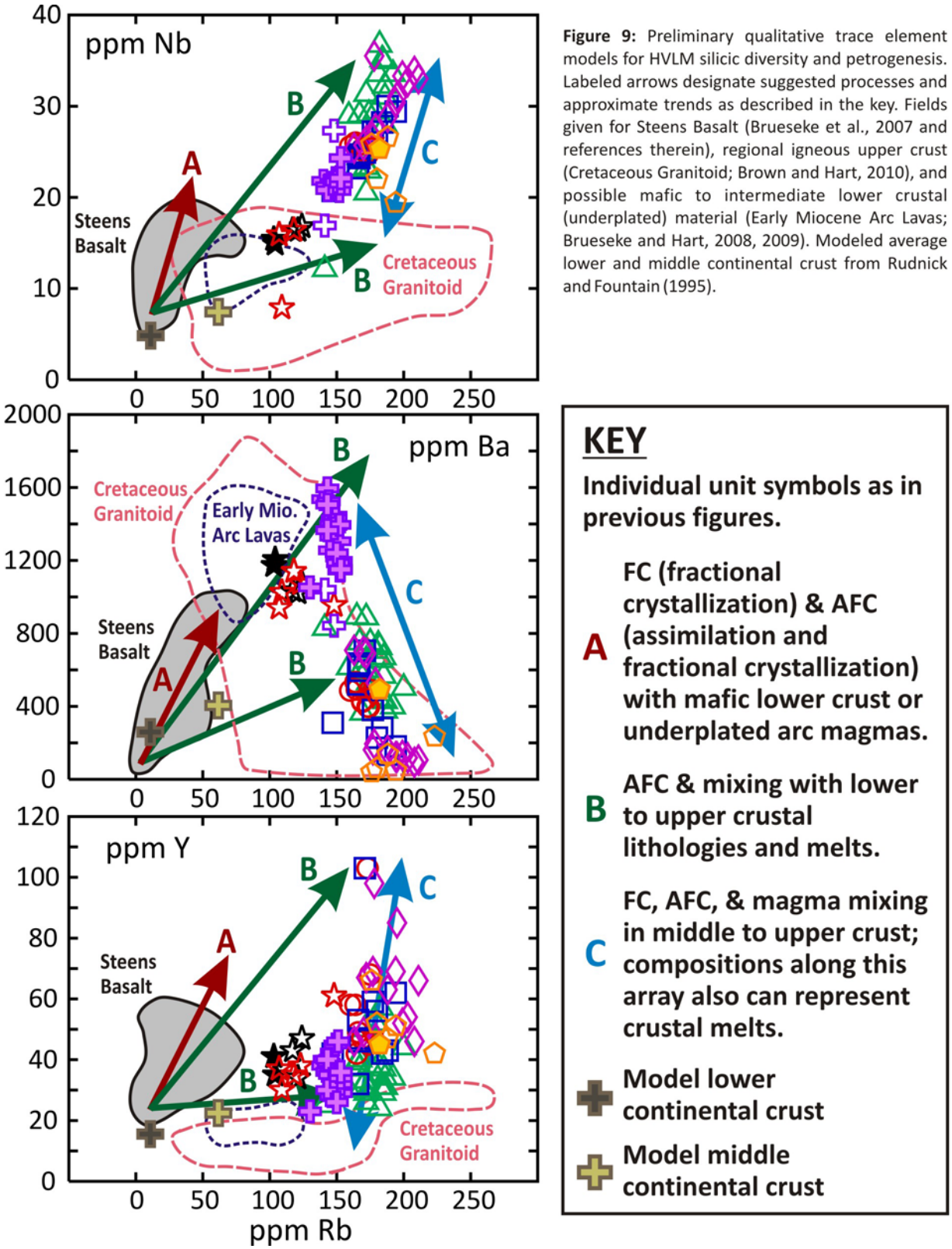

Figure 9: Preliminary qualitative trace element models for HVLM silicic diversity and petrogenesis. Labeled arrows designate suggested processes and approximate trends as described in the key. Fields given for Steens Basalt (Brueseke et al., 2007 and references therein), regional igneous upper crust (Cretaceous Granitoid; Brown and Hart, 2010), and possible mafic to intermediate lower crustal (underplated) material (Early Miocene Arc Lavas; Brueseke and Hart, 2008, 2009). Modeled average lower and middle continental crust from Rudnick and Fountain (1995).

FAULTING AND VOLCANISM

In this section key structural observations and interpretations are briefly summarized with an emphasis on the coincidence of faults and fault intersections with eruptive localities. The HVLM map area is characterized by major NNE- and NW-striking faults with substantial normal dip-slip displacement offsetting the Quaternary mafic and mid-Miocene silicic units by an average of ~100m (range from ~10m to 300m). Measurements of total offset for the NW-striking normal faults are difficult to make because alluvium and/or young basalt often covers the silicic units of a hanging wall. The dip of the faults also is not well established because of a lack of exposed fault planes. Fault plane measurements close to the area of interest reveal high angle displacements; for example: ~60° near Steens Mountain (Fuller and Waters, 1929), and 60° to 90° at Summer Lake (Donath, 1962). Seismic data also indicate that high-angle normal faults dominate in this portion of the HLP-NWBR transition (Ludwin et al. 1991). We interpret a uniform fault dip of ~75-80° from available data for regional fault systems (references above and Scarberry et al., 2010) as well as steep slopes along the fault scarps displacing the volcanic units of the HVLM map area. NNE-trending faults display a typical average strike of ~15°, ranging from ~0° to as much as ~60-70° within Funnel Canyon (Plate 1). These structures cut the Quaternary basalts as well as the older silicic units. The NW-trending faults (~300-330°), with rare exception, cut only the silicic units and typically disappear below young basaltic cover. The relationship of the presently observable NW-striking faults to the silicic and mafic units indicate that the faults had to be active after final emplacement of the silicic units at ~16 Ma; however the faulting cannot be younger than the emplacement of the HVLM basalts beginning at ~0.8 Ma. Moreover, the location of silicic vent areas along or in close proximity to these structures suggests that the current features formed along previous structural discontinuities. The relationships between the NNE-trending faults, mafic and silicic vent areas, and the mafic and silicic units that they displace indicate that these structures had to be active at 16.3±0.3 Ma and were reactivated after basalt emplacement at ~0.5 Ma. The coincidence of silicic vent areas with the intersections of NNE- and NW-trending faults (Plate 1) leads to the interpretation that both structural trends represent reactivated older (>16.5 Ma) fabrics in the crust that focused magma ascent and establishment of crustal magma chambers and that ultimately were used as paths for silicic magma transport to the surface.

CONCLUSIONS AND FUTURE DIRECTIONS

Our new mapping at the 1:24,000 scale plus associated data, coupled with previous reconnaissance mapping and geochronologic and geochemical data (Legge, 1988; Pasquale and Hart, 2006; Tables 1-3) indicate that the HVLM is characterized by a NW-striking structural valley that cuts an ~150 km^2 16.3±0.3 Ma, largely trachyte-trachydacite-rhyolite volcanic complex. Available radiometric ages and stratigraphic relationships indicate that the bulk of HVLM volcanism occurred during a <1 m.y. window synchronous with or shortly following eruption of the Steens basalt from fissures in the Steens-Pueblo Mountains located less than 20 km to the east. Local HVLM eruptions produced small volumes of Quaternary basalt (0.6±0.3 Ma) that were erupted along and offset by reactivated NNE-striking structures. In contrast, NW-striking faults with rare exception displace only the mid-Miocene silicic lavas and are in turn cut by NNE-striking structures. This observation that NW-striking faults formed ahead of NNE-striking faults is in agreement with a recent detailed study west of the HVLM (Scarberry et al., 2010). Numerous rhyolite-trachydacite-trachyte vents that produced physically, petrographically, and chemically distinct units are situated at or near the intersection of NNE- and NW-striking structures indicating that both structural trends were active and available for magma passage in

the mid-Miocene. In other words, mid-Miocene and younger structural features in the HVLM likely represent reactivation of older structural fabrics.

The observations and data suggest: 1) influx of regionally voluminous mantle-derived melts (Steens Basalt) starting at ~16.6 Ma provided the thermal and material inputs driving crustal modification and establishment of the HVLM silicic magmatic systems, 2) source (heterogeneous mantle and crustal melts) and process (fractional crystallization, assimilation, magma mixing) related factors are responsible for within and between vent/unit geochemical heterogeneity, 3) separate relatively small upper-level magmatic systems were established along regional lithospheric weaknesses, with their eruption likely triggered by periods of heightened regional/local tectonic or/and magmatic activity, and 4) following an ~15 Ma hiatus, HVLM volcanism reinitiated with small volume basaltic eruptions from vents along active zones of NWBR deformation, with the basalt flow field subsequently displaced by NNE-striking normal faults. Moreover these working hypotheses imply that mid-Miocene silicic magma generation and evolution in the ION region is intimately linked to the Yellowstone hotspot from a petrologic perspective. In the HVLM area, this silicic volcanism also was controlled by structural regimes common to the present day Basin and Range and High Lava Plains Provinces suggesting tectonic influences linked to reactivation of a pre-existing structural fabric associated with broader late-Cenozoic northwestern U.S. plate interactions. Thus, a picture emerges for the HVLM area that implicates a combination of regional plate tectonic and focused mantle upwelling (hot spot) influences on lithosphere modification, magma generation, establishment and emptying of crustal magma bodies, and syn- and post-magmatism lithosphere deformation.

Capitalizing on what we have learned during the work on this EDMAP project, we are currently further investigating the petrogenesis of HVLM silicic magmas in the context of new emerging regional geologic, geochemical, petrologic, and geophysical information associated with the NSF-funded High Lava Plains Project (e.g., Roth et al., 2008; Streck and Grunder, 2008; Warren et al., 2008; Meigs et al., 2009). Our continued petrogenetic studies involve additional trace element and multi-isotope system (Sr-Nd-Pb-Hf) data acquisition making use of whole rock materials, matrix glass separates (Wypych and Hart, 2010), and individual minerals displaying petrographic evidence for complex cooling/evolution histories. With the eruptive and structural history and the basic geochemical architecture of the HVLM now in hand, we are well situated to follow-up with the aforementioned petrogenetic investigation and to apply the resulting information and models to more general questions of silicic magma evolution and the interplay between tectonic and magmatic processes in continental settings.

ACKNOWLEDGMENTS

This research was supported by the U.S. Geological Survey, National Cooperative Geologic Mapping Program, under assistance Award No. G09AC00145 and the National Science Foundation Award EAR-0506887 Continental Dynamics Program, both to William K. Hart. We also acknowledge support from the Miami University Doctoral – Undergraduate Opportunities for Scholarship program to Alicja Wypych and Kelly C. McHugh. We thank Matthew Brueseke from Kansas State University for reviewing the map and cros-sections, Dr. John Morton for assistance in the geochemistry lab at Miami University and Dr. Stan Mertzman of Franklin and Marshall College for providing X-ray fluorescence major and trace element data.

REFERENCES CITED

Atwater, T. and Stock, J.M., 1998. Pacific-North America plate tectonics of the Neogene Southwestern United States - An Update: Int. Geol. Rev., 40: 375–402.

Brown, K.L. and Hart, W.K., 2010. Geochronology and geochemistry of a Late Cretaceous granitoid suite, Santa Rosa Range, Nevada: linking arc magmatism in northwestern Nevada to the Sierra Nevada Batholith: Eos Trans. AGU 91, Fall Meet. Suppl., Abstract V23B-2445.

Brueseke, M.E. and Hart, W.K., 2009. Geology and geochemistry of Early Miocene intermediate composition volcanism in northern Nevada and its relationship to regional tectonomagmatic processes. Geol. Soc. Amer. Abs. with Prog., 41: 337.

Brueseke, M.E. and Hart, W.K., 2008. Geology and petrology of the mid-Miocene Santa Rosa – Calico Volcanic Field, northern Nevada: Nev. Bur. Mines Geol. Bull., 113.

Brueseke, M.E., Hart, W.K., and Heizler, M.T., 2008. Diverse mid-Miocene silicic volcanism associated with the Yellowstone-Newberry thermal anomaly: Bull. Volcanol., 70: 343-360.

Brueseke, M.E., Heizler, M.T., Hart, W.K., and Mertzman, S.A., 2007. Distribution and geochronology of Oregon Plateau (U.S.A.) flood basalt volcanism: the Steens Basalt revisited: J. Volcanol. Geotherm. Res., 161: 187-214.

Camp, V. E., and Ross, M.E., 2004. Mantle dynamics and genesis of mafic magmatism in the intermountain Pacific Northwest: J. Geophys. Res., 109: B08204.

Carlson, R.W. and Hart, W.K., 1987. Crustal Genesis on the Oregon Plateau: J. Geophys. Res., 92: 6191-6206.

Castor, S.B. and Henry, C.D., 2000. Geology, geochemistry, and origin of volcanic rock-hosted uranium deposits in northwestern Nevada and southeastern Oregon, USA: Ore Geol. Rev., 16: 1-40.

Christiansen, R.L. and Lipman, P.W., 1972. Cenozoic volcanism and plate tectonic evolution of the western United States - Part II, Late Cenozoic: Phil. Trans. Roy. Soc. Lon., A271: 249-284.

Colgan, J.P., Dumitru, T.A., McWilliams, M., and Miller, E.L., 2006. Timing of Cenozoic volcanism and Basin and Range extension in northwestern Nevada: New constraints from the northern Pine Forest Range: Geol. Soc. Amer. Bull., 118: 126–139.

Crider, J.G., 2001. Oblique slip and the geometry of normal-fault linkage; mechanics and a case study from the Basin and Range in Oregon: J. Struct. Geol., 23: 1997-2009.

Donath, F.A., 1962. Analisys of basin-range structure, south-central Oregon. Geol. Soc. Amer. Bull., 73: 1-16.

Faulds, J.E., Henry, C.D., and Hinz, N.H., 2005. Kinematics of the northern Walker Lane: incipient transform fault along the Pacific North American plate boundary: Geology, 33: 505-508.

Fuller, R.E. and Waters, A.C., 1929. The nature and origin of the horst and graben structure of southern Oregon. J.Geol., 37: 204-238.

Green, R.C., 1984. Geologic appraisal of the Charles Sheldon Wilderness Study Area, Nevada and Oregon: US Geol. Surv. Bull., 1538: 13–34.

Hart, W.K. and Carlson, R.W., 1985. Distribution and geochronology of Steens Mountain type basalt from the northwestern Great Basin: Isochron/West, 43: 5-10.

Hart, W.K., Aronson, J.L., and Mertzman, S.A., 1984. Aerial distribution and age of low-K, high-alumina olivine tholeiite magmatism in the northwestern Great Basin, U.S.A.: Geol. Soc. Amer. Bull., 95: 186-195.

Henry, C. D., Castor, S. B., McIntosh, W. C., Heizler, M. T., Cuney, M., and Chemillac, R., 2006. Timing of oldest Steens Basalt magmatism from precise dating of silicic volcanic rocks, McDermitt Caldera and Northwest Nevada volcanic field: Eos Transactions AGU 87, Fall Meet. Suppl., V44C-08.

Jarboe, N.A., Coe, R.S., Renne, P.R., and Glen, J.M.G., 2010. The age of the Steens reversal and the Columbia River Basalt Group: Chem. Geol., 274: 158-168.

John, D.A., Wallace, A.R., Ponce, D.A., Fleck, R.L., and Conrad, J.E., 2000. New perspectives on the geology and origin of the Northern Nevada Rift, in Cluer, J.K., Price, J.G., Struhsacker, E.M., Hardyman, R.F., and Morris, C.L., (eds.), Geology and Ore Deposits 2000: The Great Basin and Beyond: Geol. Soc. Nev. Symp. Proc., 127-154.

Jordan, B.T., Grunder, A.L., Duncan, R.A., and Deino, A.L., 2004. Geochronology of Oregon High Lava Plains volcanism: Mirror image of the Yellowstone hotspot?: J. Geophys. Res., 109: B10202.

Katoh, S., Danhara, T., Hart, W.K., and WoldeGabriel, G., 1999. Use of sodium polytungstate solution in the purification of volcanic glass shards for bulk chemical analysis: Nat. and Human Act., 4: 45-54.

Lawrence, R.D., 1976. Strike-slip faulting terminates the Basin and Range province in Oregon: Geol. Soc. Amer. Bull., 87: 846-850.

LeBas, M.J., LeMaitre, R.W., Streckeisen, A., and Zanettin, B., 1986. A chemical classification of volcanic rocks based on the total alkali silica diagram: J. Petrol. 27: 745-750.

Legge, P., 1988. The bimodal basalt-rhyolite association west of and adjacent to the Pueblo Mountains, southeastern Oregon: [M.S. thesis] Miami University.

LeMaitre, R.W., 1976. Some problems of the projection of chemical data into mineralogical classifications: Contrib. Mineral. Petrol., 56: 181-189.

Lerch, D.W., Miller, E.L., McWilliams, M., and Colgan, J.P., 2008. Tectonic and magmatic evolution of the northwestern Basin and Range and its transition to unextended volcanic plateaus: Black Rock Range, Nevada: Geol. Soc. Amer. Bull., 120: 300-311.

Ludwin, R.S., Weaver, C.S., and Crosson, R.S., 1991. Seismicity of Washington and Oregon, in Slemmons, D.B., Engdahl, E.R., Blackwell, E., and Schwartz, D., eds., Neotectonics of North America: Geol. Soc. Amer. DNAG, GSMV-1: 77-98.

Meigs, A., Scarberry, K., Grunder, A., Carlson, R., Ford, M., Fouch, M., Grove, T., Hart, B., Iademarco, M., Jordan, B., Milliard, J., Streck, M., Trench, D., and Weldon, R., 2009. Geological and geophysical perspectives on the magmatic and tectonic development of the High Lava Plains and northwest Basin and Range, in Dorsey, R.J., Madin, I.P., and O'Connor, J.E., eds., Volcanoes to Vineyards: Geologic Field Trips through the Dynamic Landscape of the Pacific Northwest: Geol. Soc. Amer. Field Guide, 15: 435-470.

Mertzman, S.A., 2000. K-Ar results from the southern Oregon - northern California Cascade Range: Ore. Geol., 62: 99–122.

McHugh, K., Wypych, A., Hart, W.K., and Scarberry, K., 2010. Geology and petrology of the Hawks Valley-Lone Mountain volcanic complex, southeastern Oregon: Geol. Soc. Amer. Abs. with Prog., 42: 62.

Pasquale, S. and Hart, W.K., 2006. The tectonomagmatic development of a mid-Miocene silicic eruptive center near the Oregon Plateau-Basin and Range boundary, SE Oregon: Geol. Soc. Amer. Abs. with Prog., 38: 94.

Pezzopane, S.K., and Weldon, R.J., 1993. Tectonic role of active faulting in central Oregon: Tectonics, 12: 1140-1169.

Pierce, K.L. and Morgan, L.A., 1992. The track of the Yellowstone hotspot; volcanism, faulting and uplift: Geol. Soc. Amer. Mem., 79: 1-53.

Pierce, K.L. and Morgan, L.A., 2009. Is the track of the Yellowstone hotspot driven by a deep mantle plume? — Review of volcanism, faulting, and uplift in light of new data: J. Volcanol. Geotherm. Res., 188: 1–25.

Renne, P.R., Deino, A.L., Walter, R.C., Turrin, B.D., Swisher, C.C., Becker, T.A., Curtis, G.H., Sharp, W.D., and Jaouni, A.R., 1994. Intercalibration of astronomical and radioisotopic time: Geology, 22: 783-786.

Roth, J.B., Fouch, M.J., James, D.E., and Carlson, R.W., 2008. Three-dimensional seismic velocity structure of the northwestern United States: Geophys. Res. Lett., 35: L15304.

Rudnick R. L. and Fountain D. M., 1995. Nature and composition of the continental crust: a lower crustal perspective: Rev. Geophys., 33: 267–309.

Rytuba, J.J. and McKee, E.H., 1984. Peralkaline ash flow tuffs and calderas of the McDermitt volcanic field, southeast Oregon and north central Nevada: J. Geophys. Res., 89: 8616-8628.

Scarberry, K.C., Meigs, A.J., and Grunder, A.L., 2010. Faulting in a propagating continental rift: Insight from the late Miocene structural development of the Abert Rim fault, southern Oregon, USA: Tectonophys., 488: 71–86.

Steiger, R.H., and Jäger, E., 1977. Subcommission on geochronology: Convention on the use of decay constants in geo- and cosmochronology: Earth Planet. Sci. Lett., 36: 359-362.

Stewart, J.H., 1998. Regional characteristics, tilt domains, extensional history of the late Cenozoic Basin and Range province, western North America, in Faulds, J.E., and Stewart, J.H., eds., Accommodation zones and transfer zones: The regional segmentation of the Basin and Range province: Geol. Soc. Amer. Special Paper, 323: 47–74.

Streck, M.J. and Grunder, A.L., 2008. Phenocryst-poor rhyolites of bimodal, tholeiitic provinces: the Rattlesnake Tuff and implications for mush extraction models: Bull. Volcanol., 70: 385-401.

Walker, G.W., and MacLeod, N.S., 1991. Geologic map of Oregon: U.S. Geol. Surv., Reston, VA.

Warren, L.M., Snoke, A.J., and James, D.E., 2008. S-wave velocity structure beneath the High Lava Plains, Oregon, from Rayleigh-wave dispersion inversion: Earth Planet. Sci. Lett., 274: 121-131.

Wesnousky, S.G., 2005. The San Andreas and Walker Lane fault systems, western North America: transpression, transtension, cumulative slip and the structural evolution of a major transform plate boundary: J. Struct. Geol., 27: 1505–1512.

Wypych, A. and Hart, W.K., 2010. Mid-Miocene silicic volcanism in the Idaho-Oregon-Nevada region as a window into continental crust formation and modification. Geol. Soc. Amer. Abs. with Prog., 42: 96.

Wypych, A., Scarberry, K.C., Flores, L., McHugh, K., and Hart, W.K., 2009. Volcanotectonic development along the High Lava Plains – Basin and Range transition in southern Oregon: preliminary results of a 2009 EdMap project: Geol. Soc. Amer. Abs. with Prog., 41: 282.

Zoback, M.L., McKee, E.H., Blakely, R.J., and Thompson, G.A., 1994. The northern Nevada rift: Regional tectono-magmatic relations and middle Miocene stress direction: Geol. Soc. Amer. Bull., 106: 371-382.